

Semi-automatic mapping of shallow landslides using free Sentinel-2 and Google Earth Engine.

Davide Notti.¹, Martina Cignetti.¹, Danilo Godone.¹, Daniele Giordan.¹

¹Institute for Geo-Hydrological Protection (IRPI), Italian National Research Council (CNR), Torino, Strada Delle Cacce 73, 10135, Italy

Correspondence to: Danilo Godone (danilo.godone@irpi.cnr.it)

Abstract. The global availability of Sentinel-2 data and the widespread coverage of free-cost and high-resolution images nowadays give opportunities to map, at low-cost, shallow landslides triggered by extreme events (e.g., rainfall, earthquake). A ~~rapid~~Rapid and low-cost shallow landslides mapping could improve ~~damages~~damage estimations, susceptibility models or land management.

This work presents a semi-automatic methodology to map potential shallow landslides (PL) using Sentinel-2 images. The PL aim to detect the most affected areas and ~~it is the first step toward more detailed~~focus on them an high-resolution mapping ~~and further investigations~~. We create a GIS-based and user-friendly methodology to extract PL based on pre-post-event NDVI variation and geomorphological filtering. The semi-automatic inventory was compared with benchmark landslides inventory drawn on high-resolution images. We also used the Google Earth Engine scripts to extract the NDVI time series and make a multi-temporal analysis.

We apply this to two study areas in NW Italy ~~hatted~~, ~~hit~~ in 2016 and 2019 by extreme rainfall events. The results show that the semi-automatic mapping based on Sentinel-2 allows detecting the majority of shallow landslides larger than satellite ground pixel (100 m²). PL density and distribution ~~well~~ match well with the benchmark. However, the false positives (30% to 50% of cases) are challenging to filter, especially when they correspond to river bank erosions or cultivated land.

Keywords: NDVI, Google Earth Engine, ~~rapid mapping~~, Sentinel-2, Extreme rainfall event, Free-cost satellite images, Shallow landslides inventory.

1. Introduction

One of the recent and forecasted impacts of climate change is the rise of extreme meteorological events (IPCC, 2014). ~~During flash floods, extreme rainfall,~~ one of the most common phenomena is the activation of shallow landslides (~~Gariano and Guzzetti, 2016~~); (Gariano and Guzzetti, 2016; Guzzetti et al., 2004; Caine, 1980). Unfortunately, shallow landslides are not triggered only by rainfall but also by other extreme events like earthquakes (Sassa et al., 1996) or rapid snow melting (Cardinali et al., 2000). These slope instabilities usually involve soils and superficial deposits and represent a meaningful impact on infrastructures (e.g., roads network) and cultivated areas. The pervasive distribution of these phenomena on slopes, hereafter mentioned as extreme events, makes their identification and mapping crucial for effective damage evaluation. For this reason, the definition of procedures and strategies aimed ~~to map~~at mapping shallow landslides has been deeply investigated in the last decades to reach different final goals like: i) the mapping of the full extent of a landslide disaster (Guzzetti et al., 2004); ii) geomorphological and erosion studies (Fiorucci et al., 2011); iii) the validation

Commentato [ND1]: R2. L12: it is the first step towards [...] --> unclear

Commentato [ND2]: R2 Hatted > Hit

Commentato [ND3]: R2 : L19: well match --> match well

Commentato [ND4]: R2: L25: during flash floods [...] shallow landslides --> what is the typical depth range of what you define shallow landslide? Also, flash floods and shallow landslides are two different phenomena both related to extreme rainfall events, they can happen simultaneously but I would not connect them directly

of susceptibility models (Bordoni et al., 2015; Cignetti et al., 2019; Rossi et al., 2010); iv) the statistical comparison of landslides inventories from different methodologies and sensors (Carrara, 1993; Fiorucci et al., 2018).

Landslide event-inventory maps are commonly implemented using several different methodologies: i) post-event aerial photos analysis and plotting (Cardinali et al., 2000); ii) manual or automatic identification based on the use of high-resolution digital elevation models (DEMs) obtained from airborne LiDAR surveys done after the event (D'Amato Avanzi et al., 2015) (Giordan et al., 2017); iii) traditional geomorphological field surveys (Pepe et al., 2019). In the last recent years, even satellite images have been used to identify and map shallow landslides (Ghorbanzadeh et al., 2021; Lu et al., 2019; Martha et al., 2010; Mondini et al., 2011; Qin et al., 2018). This recent evolution has been possible thanks

to the robust improvement of satellite resolution ~~that (sub-metric for most commercial satellites), which nowadays are~~ is not so different ~~compared to from~~ aerial images (Fiorucci et al., 2019). Recent studies are mostly based on commercial high-resolution satellite images. The use of these commercial images often requires ~~a dedicated~~ committed acquisition planning after the event that needs a high cost and limits the use of these systems. For instance, areas with low human or infrastructure presence are often overlooked by authorities that mainly dedicate funds to study more inhabited sectors. The scarcity of resources creates a bias between high-income populated areas and remote areas or developing countries that cannot afford the cost.

In the last years, the Sentinel satellites constellation of the Copernicus program made available medium-high resolution images (about 10 m) both multi-spectral (Sentinel-2) and SAR (Sentinel-1) free of cost, and with a high-frequency revisit. In addition, several areas of the world are covered by multi-temporal very-high-resolution images of GoogleEarth™ that could help to detect and map shallow landslides when pre- and post- event images are available (Borrelli et al., 2015). Google Earth Engine (GEE) cloud processing (Gorelick et al., 2017) could also be used to create time series of several satellite data (Optical, SAR), which are useful to detect the change and the recovery of vegetation and to map landslides and their effect on vegetated areas (Scheip and Wegmann, 2021; Yu et al., 2018; Handwerger et al., 2022; Lindsay et al., 2022; Ganerød et al., 2023).

In this work, ~~leveraging on the study, we utilized pre- and post-event NDVI based on (Normalized Difference Vegetation Index) data from Sentinel-2 data, we implemented to develop a dedicated methodology to detect for semi-automatically detecting potential shallow landslides semi-automatically. The presented methodology aims to be a user-friendly tool, based on free data and open source software (Notti et al., 2018), easy to replicate for other regions affected by shallow landslides. We subsequently~~. To assess the accuracy of our approach, we compared the potential landslides detected using our method with a benchmark inventory; manually mapped on post-event high-resolution images. ~~By exploiting We utilized the Google Earth Engine (GEE, we also create) platform to generate NDVI time series aimed at identifying the most suitable images, which allowed us to pinpoint the optimal image pairing for detecting potential landslides and monitoring, calculate multi-temporal NDVI averages, and keep track of vegetation recovery/growth in the affected areas. Finally, the comparison with other ancillary data allowed us to make some statistics about landslides distributions and density and the triggering factors impacted regions.~~

Our methodology aims to provide a more user-friendly approach compared to similar studies. We achieved this by using free-cost data, open-source software, and empirical thresholding, which makes it easier to replicate our approach in other regions affected by shallow landslides. The implemented methodology has been tested in two areas of north-western Italy hit by extreme rainfall events in recent years, *i.e.*, November 2016 and October 2019. The two events triggered hundreds of shallow landslides in small areas, causing widespread damage to the road network, cultivation and, in some cases, urban areas.

Commentato [ND5]: R2. L41: satellite images resolution nowadays is not so different [...] --> which is the typical resolution

Commentato [ND6]: L43: what do you mean for dedicated acquisition planning? Aren't satellite orbits sort of fixed and so the revisiting time defined?

Codice campo modificato

Semi-automatic and manual inventories and GEE scripts are also published online and open for improvement by the scientific and user community.

2. Study areas

The two presented case studies are located in NW Italy, and were respectively, affected by two heavy rainfall events in November 2016 and October 2019.

The 2016 event area (about 350 km²) is located in the Ligurian Alps at the border between Liguria and Piemonte regions (NW Italy). The shape and the extension of the study area (Figure 1) are a combination of: i) the area most hit by rainfall, ii) other literature studies of the event (Cremonini and Tiranti, 2018; Pepe et al., 2019), iii) the footprint of the available Sentinel-2 cloud-free images and the post-event Google Earth image. The area of interest (AOI), henceforth called Tanarello and Arroscia valleys, shows an elevation up to 2500 m a.s.l., and a wide range of land use and vegetation cover from the Mediterranean to the alpine environment. The area intersects several river basins, and the main catchments are the Tanaro-Tanarello, part of the Po river Basin and the Arroscia stream flowing to the Ligurian Sea. From the geological point of view (Figure 1 B), the northern sector of the area is occupied by the Briançonnaise Zone of the middle Penninic nappe. This unit is represented by limestone-dolomite, which creates steep slopes, conglomerate and volcanic formation (rhyolite). In the southern part of the area, outcropping the Helminotod flysch formations of Monte Saccarello-San Remo, made by a limestone-clay sequence, and the sandstone-siltstone sequence of San Bartolomeo formation (Lanteaume et al., 1990; Pepe et al., 2015). The Tanarello and Arroscia valleys area has a sparse human settlement and low population density, ranging from 40 to 1 inhabitant per square kilometres. Most of the inhabitants live in the town of Ormea and Pieve di Teco towns. Most of the area is occupied by broadleaf forests in the lower part and coniferous forest, grassland and pasture at high altitudes.

The area affected by the heavy rainfall event in 2019 (about 530 km²) is located between the Bormida river and Lemme valleys, in the Southern-east Piemonte region. The considered area has been delimited considering the effects of the event based on the rainfall data, image coverage and reports on damages. The study area mostly overlaps with the Tertiary Piedmont Basin (TPB): a sedimentary succession from Oligocene conglomerates in the South to Pliocene mudstone in the Northern part (Figure 2 B). Three main geological formations outcrop in the detailed training areas, from South to North: the Cortemillia formation (made by Arenite, Mudstone); the Cessole Marls (made by carbonate-rich mudstone, arenite); the Serravalle Formation (made by arenite and sandstone). The southern part is occupied by ophiolitic rocks of the Ligurian oceanic unit (Piana et al., 2017). Alluvial quaternary deposits occupy the bottom of the valley. Several small creeks cross the study area with S-N directions that, in the 2019 event, caused flash floods (Mandarino et al., 2021). The geomorphology of the area is characterized by the presence of a gentle hilly landscape with a more steep characterizes the geomorphology of the area. However, the slope is steeper in the northern sector than in the rest of the training area, where the Serravalle Formation, in the northern sector, outcrops. The vineyards (region of Gavi grape) are mainly located in the central and southern portions of the study area (Cessole Marl formations). In contrast, the northern-western part is mainly covered by broadleaf forest, sclerophyllous vegetation and shrubs. Several villages and the small town of Gavi are located inside the AOI, henceforth called Gavi area. The shallow landslides frequently hit the Castle of Gavi hill was particularly hit by shallow landslides, as also occurred, like in 2014, 1977 and 1935 events (Govi, 1978; Mandarino et al., 2021).

From the climatological point of view, (Fratianni and Acquotta, 2017) Tanarello/Arroscia is between the Alpine and Liguria- Tyrrhenian climate area, while the Gavi area is between Po Plain and Upper Adriatic Region and Alpine and

Commentato [ND7]: R2: In the study area Section, I suggest to add a climatological setting description particularly (but not only) focused on extremes frequency and its possible variation in recent years.

Commentato [ND8]: L94: more steep slope in Serravalle Formation --> more steep slope than what

Liguria- Tyrrhenian zone. Moreover, the area of Gavi is also close to the area with high-frequency of intense rainfall (Fратиanni and Acquotta, 2017) in the NE sector of Liguria.

Recently, global warming and the related sea temperature increase caused a likely positive trend of extreme rainfall events in the area of the Ligurian sea, especially on a short time interval (i.e. <24 hours) (Gallus Jr et al., 2018; Paliaga and Parodi, 2022; Roccati et al., 2020).

2.1 The 20-25 November 2016 event in Tanarello and Arroscia valleys.

Historical information tells us that the Liguria region and NW Alps have been usually affected by several extreme rainfall events, usually during autumn (D'Amato Avanzi et al., 2015; Cevasco et al., 2014; Ferrari et al., 2021; Roccati et al., 2018; Guzzetti et al., 2004; Luino, 1999). Recently, global warming and the related sea temperature increase caused a likely positive trend of extreme rainfall events in the area of the Ligurian sea, especially on a short time interval (Gallus Jr et al., 2018; Paliaga and Parodi, 2022; Roccati et al., 2020).

From 20 to 25 November 2016, a low-pressure area affected the western Mediterranean Sea (Nimbus Web Eventi Meteorologici, 2022), causing heavy and persistent rainfall that hit NW Italy, and with high severity, the Ligurian Alps. The upper valleys of Tanarello and Arroscia streams (at the border between Liguria and Piemonte regions) were the most hit by this event, and the rainfall accumulation reached 650 – 700 mm (Figure 1 C). The rain gauge station of Piaggia peak up toreached a value of 690 mm over five days, which is far higher than previous floodextreme events of the last 70 years (Figure 1 D). The dense network of rainfall gauges of ARPA Piemonte and ARPA Liguria (the regional agencies for environmental protection) allowed to create an almost accurate 1 km spatial resolution map of accumulated rainfall and compare time-series of precipitation time series for some stations.

This heavy rainfall triggered many shallow landslides partly mapped with field surveys in Arroscia valley (Pepe et al., 2019). Also, deeper landslides were triggered, like in the case of the villages Monesi di Mendatica, which were partly destroyed by such kind of landslide (ARPA Piemonte, 2018; Notti et al., 2021)(ARPA Piemonte, 2018; Notti et al., 2021). Despite the limited human presence, the damages are estimated in several Millions of Euros only for public infrastructures.

Commentato [ND9]: In the study area Section, I suggest to add a climatological setting description particularly (but not only) focused on extremes frequency and its possible variation in recent years.

Commentato [ND10]: R2. L105: Especially on a short time interval --> unclear, please quantify the short time interval.

Formattato: Italiano (Italia)

Commentato [ND11]: L102: NW Alps have been affected --> always? Recently? Has the frequency changed with time? Some of this should be included in the climatological setting to be added in the study area section

Commentato [ND12]: R2: L109: 650-700 mm --> in what time? Five days

Commentato [ND13]: L112: almost accurate --> what is it meant for almost? Which method was used?

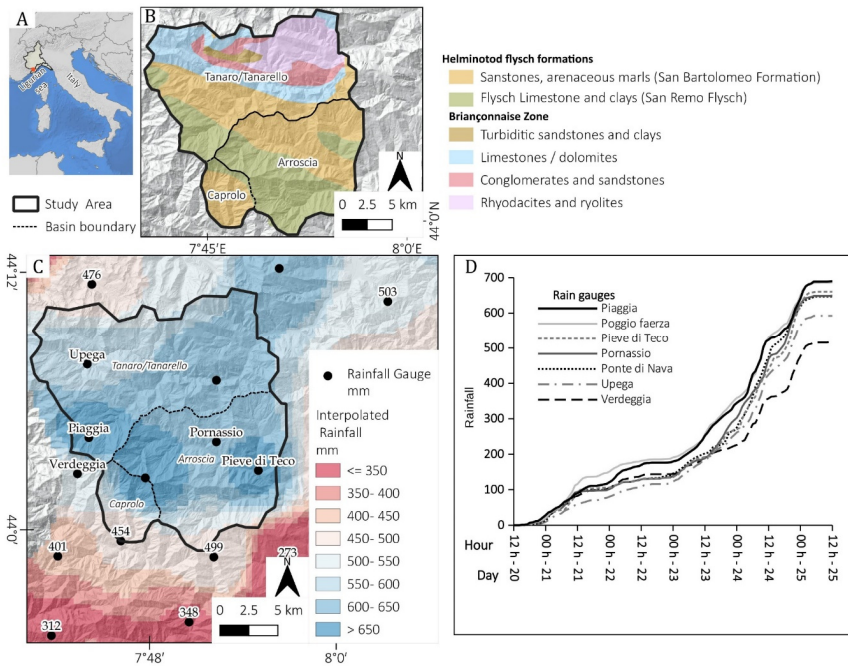
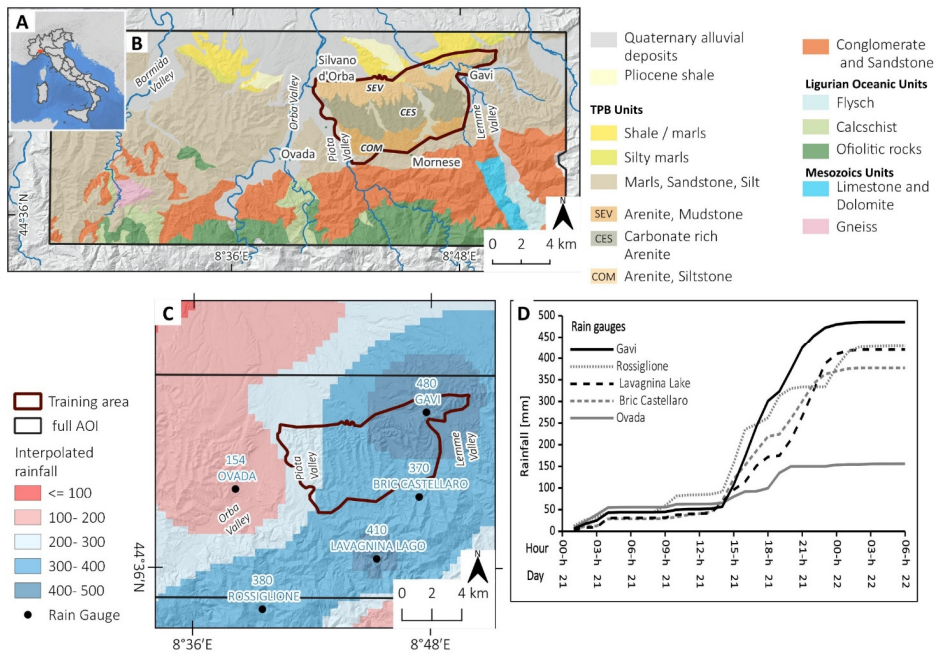


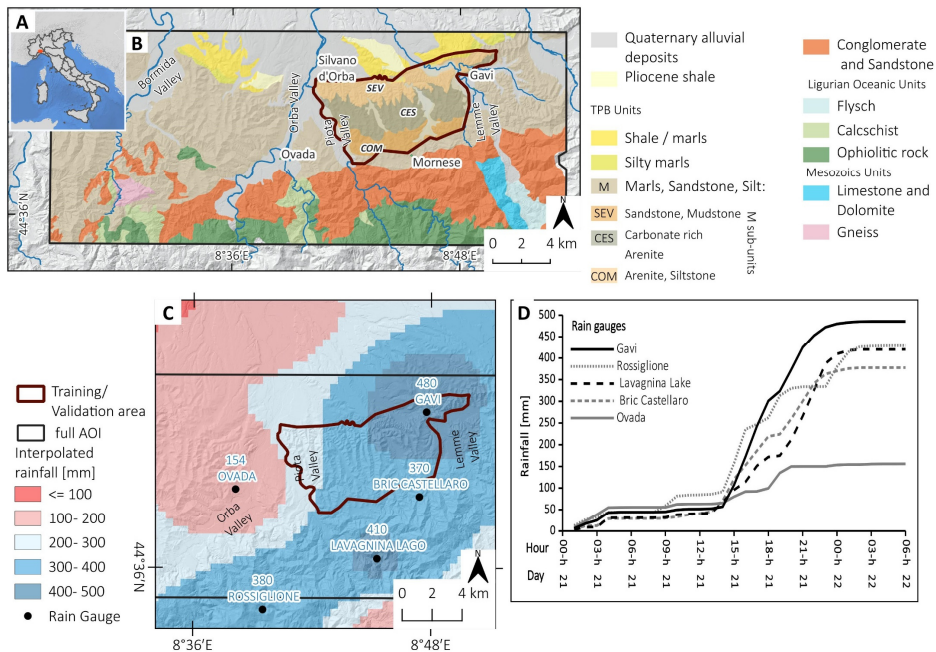
Figure 1. Arroschia/Tanarello November 2016 event. A) Location of the study area; B) Simplified geological map based on (Lanteaume et al., 1990); C) Accumulated rainfall from 20 to 25 November 2016 in the study area. D) Hourly cumulated rainfall for some rain gauge stations of study areas. (Rainfall source: ARPA Piemonte and ARPAL Liguria). Shaded reliefs of maps B and C are based on the DTM of ARPA Piemonte and Regione Liguria.

2.2 the 21-22 October 2019 event in Gavi area.

The October to December 2019 period has been characterized by numerous meteorological events that hit NW Italy, causing an extreme rainy period (Copernicus Climate Change Service, 2019). In particular, on 19-21 October 2019, an extreme rainfall event hit an area between Liguria and Piemonte regions, causing severe floods and diffuse shallow landslides in the basins of the Orba and Bormida rivers (Mandarino et al., 2021). This event was caused by a semi-stationary V-shape storm over a relatively small area with extreme rainfall (Figure 2 C) both in hourly intensity and quantity-total accumulation (Mercalli, 2019). This event activated many shallow and deep landslides. In particular, we focused on the area near the town of Gavi where the rain gauge registered about 480 mm/24h, and most of the rainfall (318 mm) was concentrated in six hours intervals (Figure 2 D) (Meteologix, 2022). It is one of the highest rainfall records in the Piemonte region, just five years after that, a previous before (October 2014), extreme rainfall hit the same area. The extreme rainfall events of autumn 2019 caused estimated damages of 16 M of Euros in the province of Alessandria (Regione Piemonte - flood events 2019, 2021). After the October 2019 event, a particularly wet period until December 2019 triggered other shallow landslides in the study area until December 2019.

Commentato [ND14]: 1.L129: intensity --> hourly intensity or instantaneous intensity?





160 **Figure 2.** Gavi October 2019 Event. A) Location of the study area; B) Simplified lithological map of the study area based on (Piana et al., 2017); C) Accumulated rainfall from 21 to 22 October 2019 event. D) Hourly cumulated rainfall for some rain gauge stations of study areas. (Rainfall data source: ARPA Piemonte, Hillshade). Shaded reliefs of maps B and C are based on the DTM of ARPA Piemonte and Regione Liguria.

165 **3. Materials and Methods.**

One of the main effects caused by the activation of shallow landslides is the reduction of vegetation cover that creates a radiometric signature variation often detected by multispectral satellites. Thus, the NDVI is one of the most used band indexes to detect these variations (Fiorucci et al., 2019; Lu et al., 2019; Mondini et al., 2011). For this reason, we create a semi-automatic methodology that deals with pre- and post-event NDVI variation based on free satellite images with the best spatial resolution (Sentinel-2, nowadays).

170 Our methodology, resumed in Figure 3, aims to produce an inventory of potential shallow landslides (PL) based on NDVI and geomorphological filters. The proposed method identifies areas most affected by the potential high-density shallow landslides that can furtherly landslide areas, and then the semi-automatic inventory will be further used to support the identification and manual mapping of landslides on very- high-resolution images. Time series of NDVI computed on GEE were also used to evaluate the vegetation recovery.

175 **3.1 Potential landslides detection methodology**

The proposed methodology (Figure 3) is aimed to create a PL inventory based on the semi-automatic procedure. The mapping method is based on the availability of pre- and post-event moderate resolution (10 m) satellite images. This methodology is intended to detect surface changes, which are signs of potential shallow landslides, between pre- and post-

Formatto: Didascalia;Didascalia_NHESS

Commentato [ND15]: L149-150: the difference between a map of areas most affected by landslides and a map of landslides is the difference between generally unstable areas and single landslides?

180 event images. The PL inventory is aimed to delimit the area most affected by shallow landslides and support a subsequent, detailed landslide mapping on very high-resolution (< 1 m) images-- (satellite or aerial based). The PL is not a geomorphological landslide inventory because the shape of PL is extracted with a semi-automatic procedure and based on middle-resolution images. The PL inventory is created in three main steps: i) satellite images selection; ii) calculation of the Normalised Difference Vegetation Index variation (NDVI_{var}), and definition of empirical NDVI_{var} threshold that is adopted for the potential landslide mapping; iii) implementation of a filter using slopesay terrain and other geomorphological parametersproperties slope to obtain the potential landslide (PL) inventory and the PL density maps. Thus, the PL inventory is compared over a training area covered by high-resolution images, with a manually drawn dataset, i.e., manual landslides (ML). This comparison phase is important because is used for checking the efficiency of PL methodology and refining the calibration of adopted parameters with iteration processes to improve the quality of the final PL inventory, reducing errors. The proposed methodology is exclusively based on free-cost software (e.g. QGIS (QGIS Association., 2022)(QGIS Association., 2022), SAGA GIS (Conrad et al., 2015), R(R Core Team., 2020)(R Core Team, 2020)) and cloud computing (e.g. GEE). In the following sections, the procedure is discussed in more detail.

Commentato [ND16]: R2: L154-157: please specify the resolution difference between satellite images and high-resolution images. Also, which is the source of high-res images?

Commentato [ND17]: L161: using slope and other geomorphological parameters --> In this phase I would say terrain and geomorphological properties.

3.1.1 Satellite Image selection.

195 The first step is the selection of the best pairs of pre- and post-event satellite images aimed to makeat making a change detection analysis. Nowadays, the free satellite images with the best resolution are Sentinel-2 (10 m visible and near-infrared bands) followed by Landsat ones (30 m).

We search for images and filter images using the following criteria:

1. cloud cover < 5%;
2. images acquired in the same period of the year to minimise the effect of shadow and canopy cover change related to season;
3. only summer images (from June to September, in N Emisphere) to havethe season with the highest NDVI, to obtain the strong contrast in NDVI, no snow coverage, and short shadow. The constraint period depends on local climatological conditions (e.g., summer from June to September in the middle latitude of the N Emisphere).

Commentato [ND18]: R2: L175: is the same period of the year of this point ii more restrictive than the period June-September?

205 To improve the search for the best pair of images, we also used output from a GEE processing based on the code developed by (Nowak et al., 2021). The processing calculates an-a temporally averaged NDVI time series from a satellite images collection (e.g. Sentinel-2) filtered by cloud cover, (< 5 %, or less if possible) over selected sample polygons that can be directly drawn on the satellite map interface of GEE. The time series plotted in a GEE chart can be exported to a CSV file for further filtering (e.g. replicate date removal) and analysis. We obtained a limited number of pairs of pre- and post-event images with these constraints.

Commentato [ND19]: R2: it is not very clear how the Novak algorithm takes into consideration the constraints listed in the bullet list i, ii, iii.

Commentato [ND20]: R2: L181: averaged NDVI --> spatially averaged

3.1.2 NDVI_{var} calculation and threshold

215 In the second step, we calculated NDVI_{var} by computing the NDVI variation between the pre- and post-event conditions (equation 1). The aim is to identify areas with decreased NDVI values due to vegetation removal or damage caused by shallow landslides. Using the raster calculator of QGIS software, we computed the NDVI using the NIR and the red band. In the specific case of our study areas, we used the Sentinel-2 band of NIR (Band 8) and red (Band 4) which have a spatial resolution of 10 m.

Commentato [ND21]: R1 - (2) Line 190, Eq.1, could the authors elaborate how the eq. 1 is applied to determine the NDVI value of the studied area? What is the 'pixel' size (the calculation area) for each of single NDVI?

220

$$NDVI_{VAR} = NDVI_{post} - NDVI_{pre} \text{ Where } NDVI = (NIR - Red)/(NIR + Red) \quad (1)$$

225

Then we manually select $NDVI_{var}$ threshold that best identifies changes related to landslides. This threshold does not have a fixed value. It is determined by an operator based on the visual pattern of $NDVI_{var}$, the evidence on the NDVI times series of GEE, and the calibration of the parameters based on PL/ML inventories comparison.

3.1.3 Geomorphological filtering to create PL inventory.

230

In the third step, the results coming from $NDVI_{var}$ are filtered using geomorphological parameters (Table 2). We first used the slope derived from DTM (download from Regione Piemonte and Liguria databases) to filter out the areas with a slope angle below a certain threshold. Then we manually select $NDVI_{var}$ threshold that best identifies changes related to landslides. This threshold does not have a fixed value, as reported in the literature (Höbling et al., 2015; Mondini et al., 2011). An operator manually determines it after visual assessment of $NDVI_{var}$, the comparison, on G, of NDVI times series between affected/not affected area, and the calibration of the parameters based on PL/ML inventories comparison (back analysis). For instance, in our study areas, both the visual pattern of $NDVI_{var}$ and the observation of NDVI time series suggest that the optimal threshold should be in the range of -0.20 / -0.15, but this could be different for other cases.

Commentato [ND22]: L194: manually select $NDVI_{var}$ threshold -->

235

Commentato [ND23]: 1.L195-196: the whole sentence --> It is unclear, can you please provide an example (or a couple)?

3.1.3 Geomorphological filtering to create PL inventory.

240

In the third step, the results coming from $NDVI_{var}$ are filtered using geomorphological parameters (Table 2). We first used the slope derived from DTM (download from Regione Piemonte and Liguria databases) to filter out the areas with a slope angle below a certain threshold. Also, in this case, the value is empirically based on the visual pattern and back analysis (slope distribution of ML). Then, all Specifically, to create PL, we applied this procedure: i) the raster values equal to 0 on rasters of $NDVI_{var}$ and slope are converted in a boolean raster (0-1) using the thresholds mentioned above (e.g., $B = [NDVI_{var} < -0.16 \text{ and } slope > 15^\circ]$) in a raster calculator of QGIS, in the computed raster the value 1 corresponds to the potential landslides (PL); ii) Then on QGIS, we converted the value 1 of the raster into PL vectors (polygon); iii) the median slope (always with QGIS) is calculated for each PL polygon and further filtered with a certain threshold (e.g. $> 17^\circ$); iv) the polygons are smoothed to obtain a more geomorphological shape. Additional filters may be introduced based on radiometric (e.g., removing the area in permanent shadow) or geometric parameters (e.g., removing the PL that overlaps with a riverbed). These filters based on empirical thresholds should be evaluated case by case considering the morphology, the land use and the ancillary data available in the study area. We finally obtained the final PL inventory with their centroid.

Commentato [ND24]: L202: the value is empirically based[...] --> in this case the threshold is unique, right?

245

Commentato [ND25]: R1 (3) The authors should detail how a polygon of PLs is formed?

250

Commentato [ND26]: 1.R2: L203-204: additional filters maybe introduced such as? In addition, maybe based on what? It's a bit obscure.

255

We used the PL centroid to create with QGIS a Kernel (Terrell and Scott, 1992) heatmap relative density (KD) map of relative PL. The PL KD aims to identify the most affected area. The parameters (e.g., search radius, size of the cell) used to generate KD maps (e.g., search radius) depend on the dimension of the study area and the average distance of PL centroids. The same procedure is applied to the ML to create a density map for inventory comparison.

Commentato [ND27]: R2: The parameters used to was a formula developed?

3.1.4 Parameters iteration calibration based on ML inventory comparison

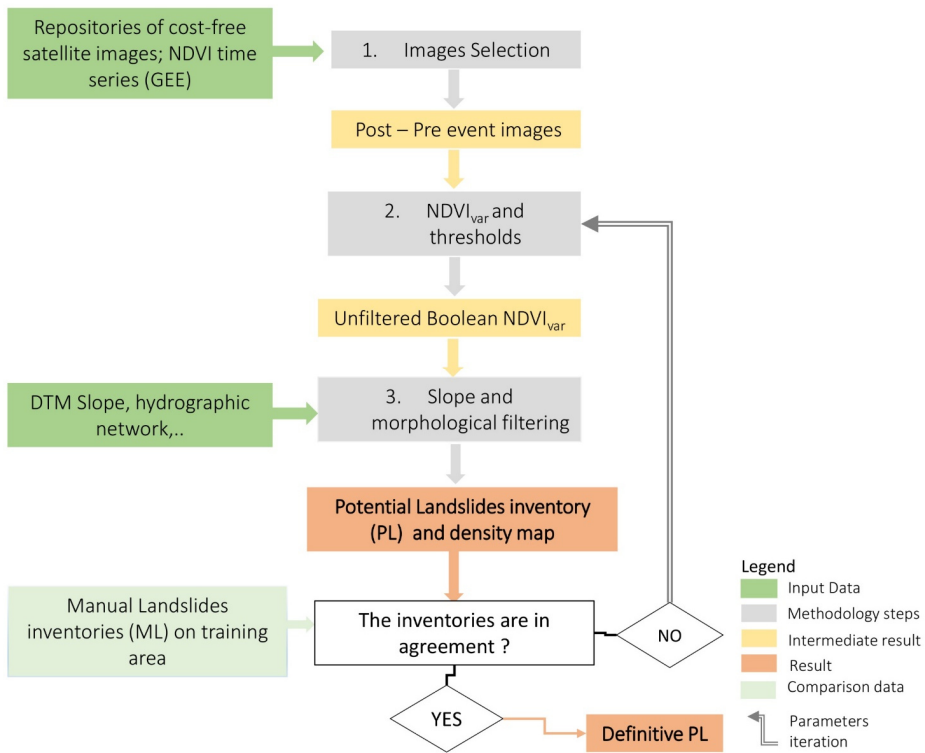
260

Usually, the manual mapping is done on a representative training area (e.g. at least 70 % of the whole AOI) (Mondini et al., 2011; Mohan et al., 2021; Trigila et al., 2013), and it is used as a benchmark dataset for calibrating the proposed method, then it is validated on a small area (30 %). In this work, having to test/validate a new methodology, we decided to operate through calibration and validation on 100% of the area of interest to determine if the technique is sufficiently robust.

The first PL inventory is then compared with a ML drawn on high-resolution images in a limited subarea of the AOI. ~~The manual mapping is done on a small training area (e.g. 10 % of the whole AOI), and it is used as a benchmark dataset for calibrating the proposed method.~~

The identification of the training area is based on the following criteria: i) availability of cost-free high-resolution post-event images, ii) PL density map, described in the previous paragraph, iii) intensity of the event (e.g., accumulated rainfall), iv) representativity of the study area in terms of lands-use and geomorphology. Once the result of the training area is available, it is possible to evaluate the statistical distribution of ML inventory in terms of $NDVI_{var}$, slope angle or other parameters for a better empirical calibration of the thresholds used to create the PL. The ~~iteration calibration~~ step aims to reduce ~~the false positivepositives~~ and ~~false negativencgatives~~ and obtain the definitive PL inventory.

Commentato [ND28]: R2: L222: The iteration step aims [...] --> when is the iteration stopped? Which is the threshold used to exit it?



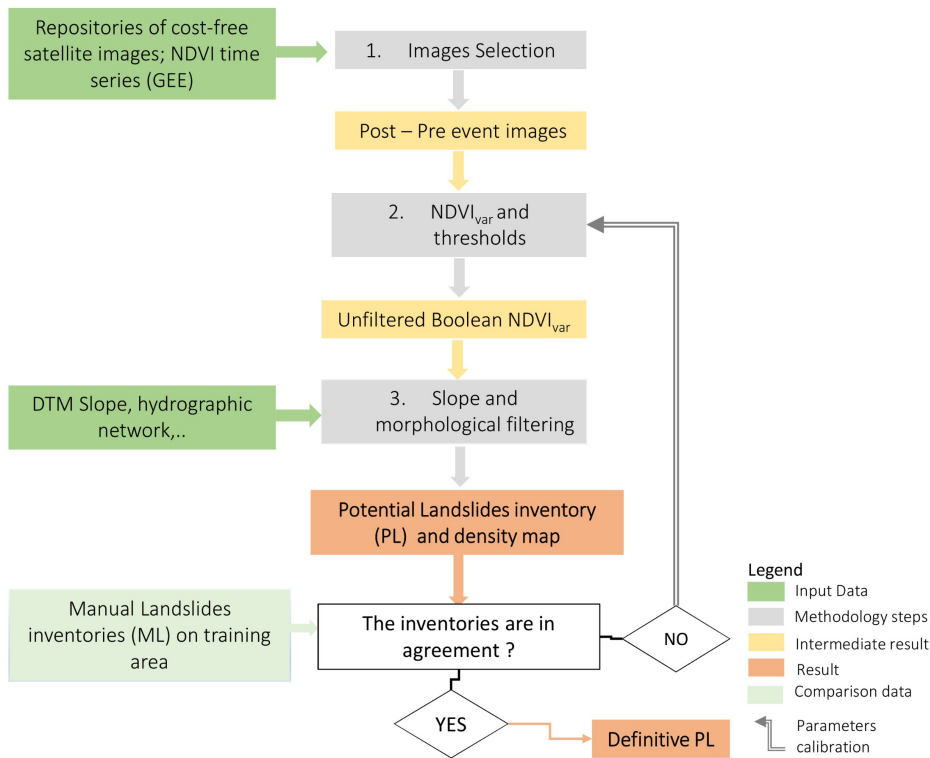


Figure 3. Flow chart of proposed shallow landslides mapping methodology.

3.2 Data, parameters and thresholds used for the case studies

280 We applied the methodology described above to our two case studies; for each, we chose the data and parameters described in the following paragraphs. The data availability section provides the link to the original databases used.

3.2.1 Satellite data and geomorphological filters

285 Following the methodology described in section 3.1, we first selected the pre- and post- images. For our case studies, we used the data of Sentinel-2 satellites (type Bottom-Of-Atmosphere reflectance in cartographic geometry - L2A) available on the Sentinel-Hub portal (Copernicus Open Access Hub, 2022). In particular, we downloaded the 10-m resolution bands visible (B2, B3, B4) and near-infrared (NIR - B8), and we clipped the original datasets on the area of interest. The dataset used in this study are listed in Table 1. For the Gavi area, we find a pair of images with one year of interval, while for Tanarello and Arroscia valley area, the best pair cloud-free is on two years interval.

290 In the second step, we defined the $NDVI_{var}$ and geomorphological thresholds. In our case study, we used $NDVI_{var} \leq 0.15$ joined to $slope > 15^\circ$ entries values to create the Boolean raster where the value 1 identifies the potential landslides. The slope models were computed from 5-m DTM available from the databases of the Piemonte and Liguria regions. The boolean raster keeps the same spatial resolution of Sentinel-2 (10x10 m pixel).

Commentato [ND29]: L239: The Boolean raster [...] --> how is this obtained? With a single 10 m x 10 m cell there are four 5 m x 5 m cells. Did you use an average value? Majority? Else?

We used additional geomorphological thresholds, such as the median slope of the PL polygons. The values were based on the statistical distribution of the ML median slope. We used the filter values median slope $\geq 17^\circ$ and $\geq 20^\circ$ for the Tanarello and Arroscia valley area and the Gavi area, respectively.

In the Tanarello and Arroscia valleys case, we removed the polygons nearby (using an empiric buffer from 5 to 10 m) the hydrographic network to remove false positives related to riverbank erosion. We also filtered the areas in a constant shadow because of a cliff, using threshold values of the averaged means of the four 10-m bands (RGB and NIR) of Sentinel-2 images. The PL polygons were finally smoothed and merged if their distance was lower than 1 m.

Table 1: Sentinel-2 images used in the selected case studies

Case study	Event date	Image Source	Band	Spatial resolution	Pre-Event images	Post-Event Images	Usage
Tanarello and Arroscia valleys	20-26 November 2016	Sentinel-2	R-G-B; NIR	10 m	23/08/2016	28/08/2018	Semi-Automatic detection
		GEE	NDVI	10 m	2016-2021		NDVI time series
Gavi area	20-26 October 2019	Sentinel-2	R-G-B; NIR	10 m	26/06/2019	20/06/2020	Semi-Automatic detection
		GEE	NDVI	10 m	2016-2021		NDVI time series

Commentato [ND30]: L247: Table 1 --> I believe it could help the reader to have the event date in the Table.

Tabella formattata

Celle inserite

3.2.2 High-resolution images for ML inventory.

For our study, we employed a stringent calibration and validation methodology in both of our study areas, with an equal ratio of 1:1. This differs from the commonly used approach in the literature of a 7:3 ratio, as reported in studies such as Mondini et al. (2011) and Mohan et al. (2021). Our decision to utilize this methodology was motivated by the fact that it was our first time implementing this approach. Furthermore, we employed a statistical validation method that is user-friendly and straightforward to replicate in future studies. For the Tanarello-Arroscia case, the training-validation area is about 300 km², while it is 50 km² for Gavi 2019 case.

Concerning the Gavi area case study, we focus the manual mapping applied the proposed methodology as in an ordinary scenario; therefore, we performed, over small training areas 10% (about 50 km²), this allows tuning of the area training and validation, and then, with the previously defined parameters to produce the PL over the whole study area (552 km²). For the Tanarello and Arroscia valleys case study, the ML training area corresponds to the entire study, we applied the method to 90% (500 km²) of the area because we decided to test the iteration step with more detail and obtain a complete semi-automatic, producing the inventory validation. The large 2019 area is also intended to be used as a test inventory for other studies.

The manual mapping of the landslides was made (in early 2022) on very high-resolution post-event images. In our case study, high-resolution images were available for both areas, dating back to a few months after the events (Table 2). We used the post-event satellite images available on Google Earth upload as XYZ tiles layer on QGIS software. We also used pre-event high-resolution orthoimages available as a web map service (WMS) on the national cartographic service of Italy or the regional web map service of Piemonte and Liguria regions.

Commentato [ND31]: R2 mian In line 251-255 authors explain that for a study area small training areas are selected while for the other case study the whole domain is used. If for the same study area, small training areas and then the whole domain are used, does the performance of the procedure change? By a sort of iteration, is it possible to define an ideal dimension of the training area? Is it possible to confirm this ideal dimension for the second area or it changes due to the different morphological and land-use conditions?

325 The manual polygons of landslides (ML) were drawn following geomorphological criteria with the help of shaded relief
DTM. Two operators manually checked the inventories to reduce the subjectivity of mapping. The landslide mapping
was made on QGIS with the support of Google Earth Pro for historical image visualisation.

Table 2. High-resolution images used for ML mapping in this work.

Case study	Image Source	Band	Spatial resolution	Pre-Event images	Post-Event Images	Usage
Tanarello and Arroscia valleys	Google Earth; National cartographic portal (PCN)	Visible	0.3 m	24/09/15 2012	03/08/17	PL Validation and Manual mapping
Gavi area	Google Earth; Piemonte regional webgis service	Visible	0.3 m	01/06/2019 2018	07/04/2020 16/03/2021	PL Validation

3.2.3 NDVI time series analysis using GEE.

330 We also used GEE's potentiality to check and compare the NDVI time series affected by shallow landslides. We manually
draw on the GEE interface some sample polygons, imported as feature collections representative of different conditions
(landslide / no landslides) and land use. As for the choice of the best images described in section 3.1, we used an
algorithm based on (Nowak et al., 2021). We also extract the NDVI time series using the GEE time-series explorer
335 QGIS plugin (GEE Timeseries Explorer), such script allows producing single-pixel TS time series directly from a point
vector. The time series analysis is aimed to estimate the recovery of vegetation recovery in the area affected by
shallow landslides and compare it with healthy areas. The vegetation recovery helps assess the maximum period in which
a post-event image can be used to calculate $NDVI_{var}$. The NDVI time series located in different land use were also
compared using GEE.

Commentato [ND32]: R2: L271-272: algorithm based on Novak et al. (2021) --> is it exactly the same algorithm described in Section 3.1 or there are some differences?

Commentato [ND33]: R2: L273: TS --> please define the acronym

Commentato [ND34]: R2: L274: estimate the recovery of vegetation --> if this is a specific objective of your study, please clarify it in the introduction.

340 3.3 PL and ML inventories comparison and statistics

We compared the PL with ML to evaluate the efficiency of semi-automatic detection by using geoprocessing tools in a GIS environment. Results were synthesized in a validation matrix (Table 3). PL and ML vector layers were merged in a unique one to obtain the intersections between the two datasets, thus getting true positive (TP), then by selecting residuals PL (i.e. parts not included in the intersection) touching or not the intersection, partial positive (PP) and false positive (FP) were detected. On the other hand, partial detection (PD) and false negative (FN) were defined, respectively, by residual ML touching the intersection sector and ML not intersecting with PL. The five categories were merged in a unique vector layer for further analysis, with the aforementioned classification stored in the attribute table.

345 The three types of intersections in which PL are involved (TP, PP and FP) were used to analyze and validate the semi-automatic methodology. Then, by overlaying them on NDVI and slope angle raster layer, mean values were calculated and stored for each feature. Those values were then processed to obtain descriptive statistics and frequency distributions in terms of the previously described categories. The ML/PL comparison of datasets was also used in an iteration process to enhance the parameters to obtain the PL. The characteristics of FP allowed improving the filters in semi-automatic detection. We use the false positive ratio (FPR, equation 2) to measure the percentage of the area not correctly

$$detectedFPR = \frac{(FP)}{[(FP) + (TP) + (PP)]} (2)$$

355 We define the detection ratio (DR, equation 3) to evaluate the efficiency of our methodology: The DR measures the percentage of shallow landslides detected by the PL methodology. We also analyse the factors influencing the DR, such as shallow landslide dimension or land use.

360 The three intersections involving PL (TP, PP and FP) were used to analyze and validate the semi-automatic methodology. Then, by overlaying them on NDVI and slope angle raster layer, mean values were calculated and stored for each feature. Those values were then processed to obtain descriptive statistics and frequency distributions in terms of the previously described categories. The ML/PL comparison of datasets was also used in an iteration process to enhance the parameters to obtain the PL. The characteristics of FP and TP (e.g. slope and NDVI_{var} distribution) allowed for improving the filters in semi-automatic detection. We applied some equations similar to those commonly used in literature (Prakash et al., 2021; Nava et al., 2022; Catani, 2021) to check the quality of automatic mapping. Thus, the false-positive rate (FPR, equation 2) measures the percentage of the area not correctly detected, and the detection rate (DR, equation 3) is the percentage of shallow landslides (both full and partially) detected by the PL methodology. We also analyse the factors influencing the DR, such as shallow landslide dimension or land use.

370

$$FPR = (FP) / [(FP) + (TP) + (PP)] (2)$$

$$DR = [(TP) + (PD)] / [(TP) + (PD) + (FN)] (3)$$

Commentato [ND35]: R2: L288: The characteristics of FP --> what characteristics?

Commentato [ND36]: R1 (4) Reference to Eq. 2 and Eq. 3 should be provided. The definitions of Eq. 2 and Eq. 3 seem to be different from other studies.

Commentato [ND37]: L294: landslide dimension or land use --> why not using terrain properties such as aspect, slope, flow accumulation?

Commentato [ND38]: 1.L296: Table 3 --> can you please clarify the difference between PP and PD? How did you distinguish between the two? Does it mean that in PP, PI is larger than ML while for PD is the opposite?

Commentato [ND39]: R2: Results should be discussed against previous literature with major detail.

Table 3. Inventories comparison matrix

Intersection type	Denomination
Area of the full intersection of PL and ML	True Positive (TP)
PL intersected by ML but not overlapping	Partial Positive (PP)
ML intersected by PL but not overlapping	Partial Detection (PD)
Detected by PL not Mapped in ML	False positive (FP)
Not Detected by PL and Mapped in ML	False negative (FN)

375 We also compare the PL and ML inventories using the KD maps made with the procedure described in paragraph 3.1.3. The two densities, sampled on the same regular grid, are compared in a scatter plot, and a correlation coefficient is calculated (Benesty et al., 2009).

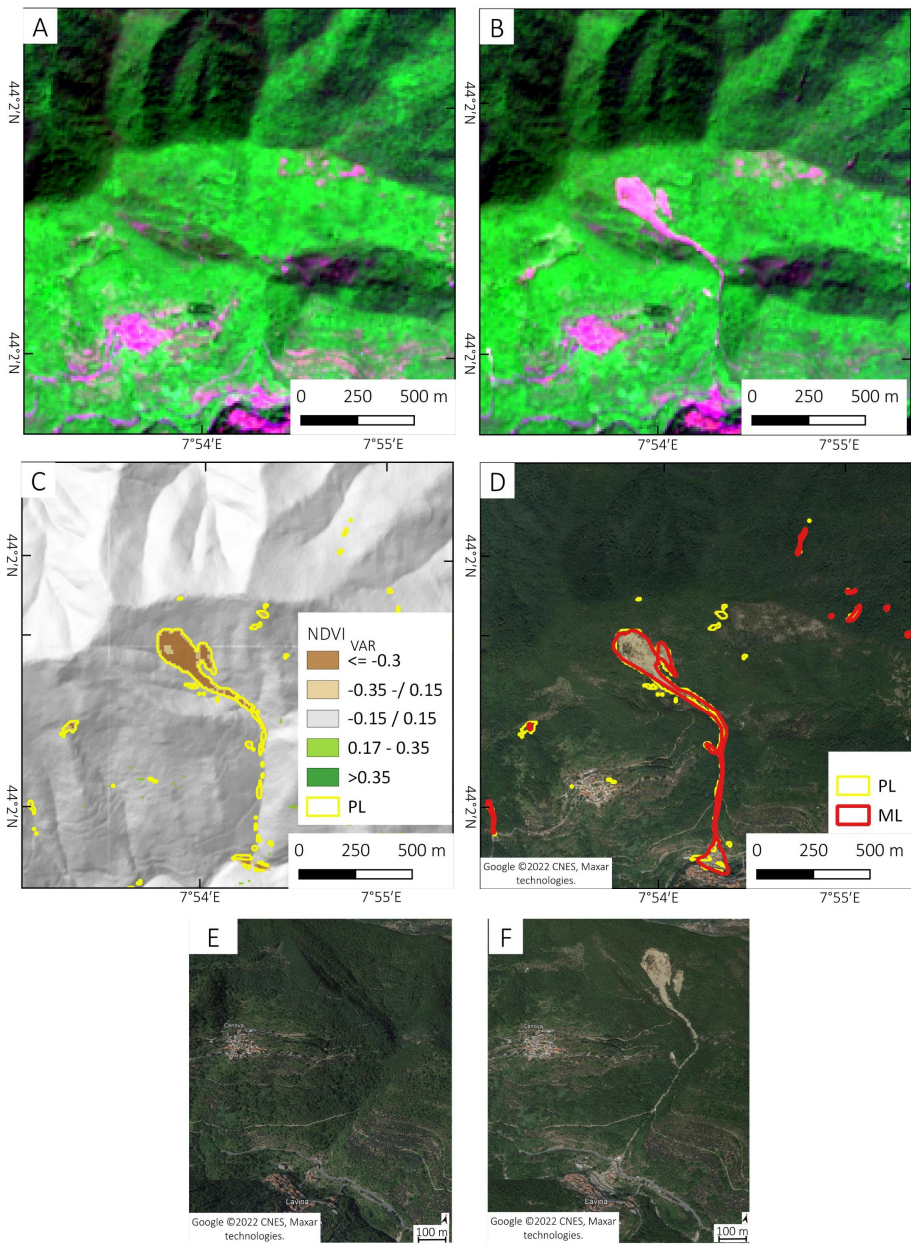
380 **4. Results and discussion**

The proposed methodology was applied to the two case studies of the Tanarello and Arroscia valleys (2016) and the Gavi area (2019). We obtained for both areas PL and ML inventories with more than 1000 shallow landslides mapped for each AOIs. The comparison of ML and PL inventories allowed us to compute statistics on the semi-automatic mapping approach's efficiency and improve parameters with iteration. We used of PL are also presented in the NDVI time series computed on GEE to evaluate the post-event vegetation recovery following paragraphs. Finally, a comparison with other ancillary datasets was made were compared to analyse shallow landslide distribution characteristics. In the supplementary material, two figures show an example of the application of our methodology step-by-step for the sampled area of the two case studies

4.1 Tanarello and Arroscia valleys study area

The semi-automatic mapping based on $NDVI_{var}$ of pre-event (2016-08-23) and post-event (2018-08-28) Sentinel-2 images, for the Tanarello and Arroscia valleys study area provided 1056 PL.

390 Figure 4 shows an example of the steps and results of our methodology over a sample area of the Arroscia/Tanarello case study. From the comparison of pre- (Figure 4 A), and post-event images (Figure 4 B), we obtained the $NDVI_{var}$ that was used to extrapolate the PL (Figure 4 C). Figure 4 D compares the ML draw on high-resolution Google Earth satellite images and the PL. A detailed 3-D view from Google Earth Pro of pre- and post-event is shown in Figures 4 E and F.



395

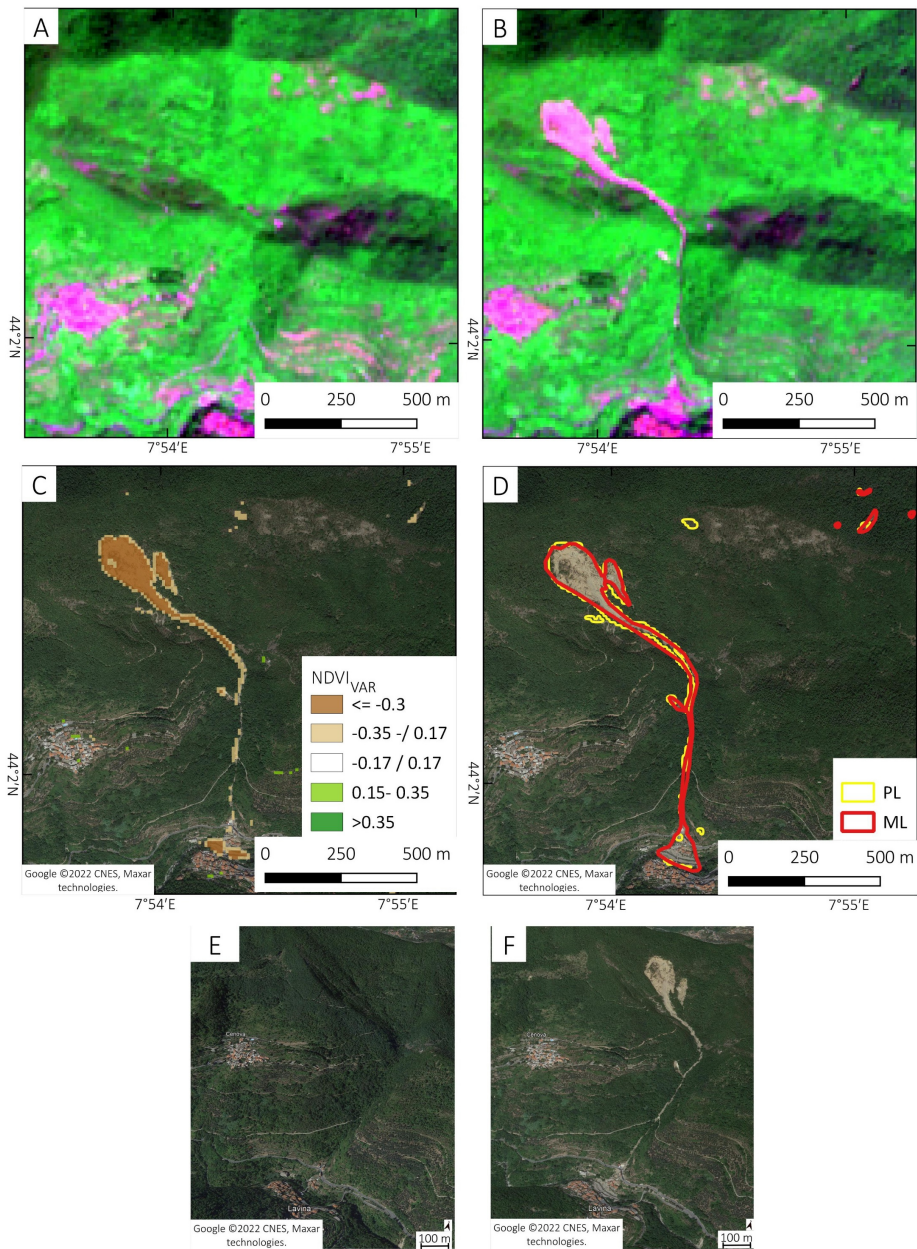


Figure 4. Example of shallow landslides detection methodology for Tanarello and Arroscia valleys case study: A) Sentinel-2 pre-event images (RED-NIR-BLUE) acquired on 2016-08-23; B) Sentinel-2 post-event images (RED-NIR-BLUE) acquired on 2018-08-28; C) $NDVI_{var}$ map PL inventory; D) ML and PL inventory overlapped to post-event high-resolution image (Google Earth – 2017). Google Earth 3D view of pre- (E) and post- (F) events of the area affected by landslides. Maps data: Google ©2022 CNES, Maxar technologies.

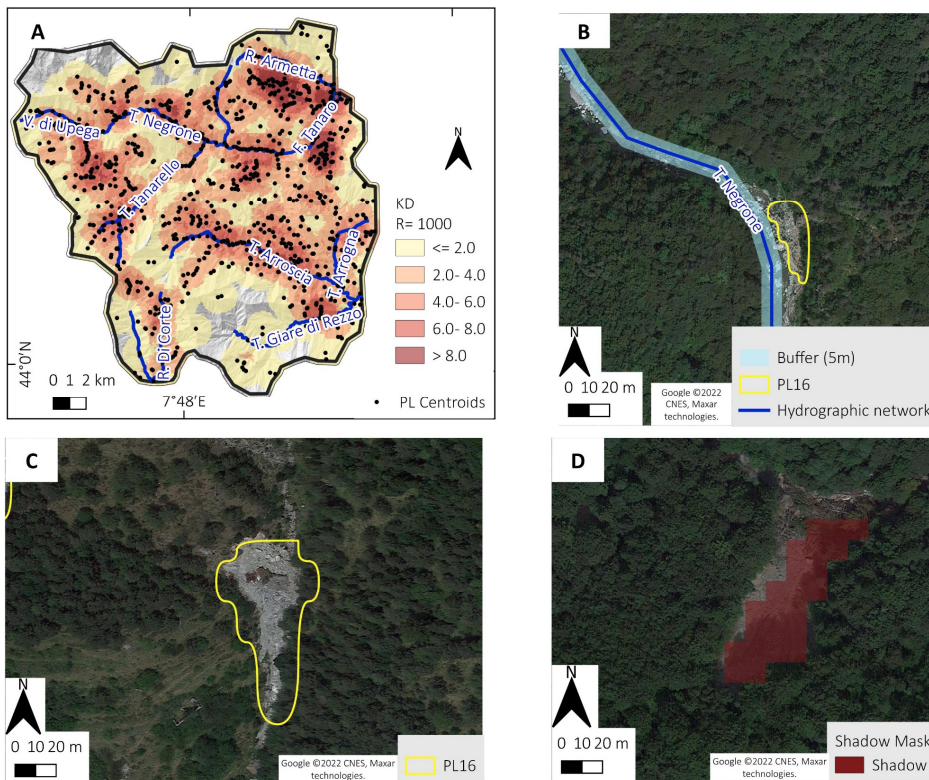
4.1.1 PL density and distribution

405 The distribution and Kernel density (KD) (search radius 1000 m) of PL centroids are shown in Figure 5 A. At the basin scale, it is possible to appreciate a high density of PL in the central sector, particularly in the Arroscia, Armetta and Tanarello valleys, where the density reaches a peak of 10 centroids / km². Moreover, Figure 5 B shows a PL detail corresponding to riverbank erosion, **not filtered out** because the hydrographic network has no precise **high-resolution geocoding**, and the derived 5m buffer did not intersect the PL. It is challenging to create an affordable geomorphological filter discriminating river erosion from a shallow landslide in a steep valley, and in many cases, the two processing overlap or are linked by a cause-effect relationship. Figure 5 C shows the correct detection of a landslide, its shape is almost accurate considering the Sentinel-2 resolution, while Figure 5 D shows a shallow landslide not detected (false negative case) because the shadow mask filters it out.

410

415

Commentato [ND40]: R2. L330: not filtered because the hydrographic network has no precise geocoding --> unclear.



415 **Figure 5.** A) The Kernel landslides centroids relative density (search radius = 2500). B) Detail of PL representing a river bank erosion; C) PL that correctly detects the shallow landslide, D) Shallow landslides not detected by PL because filtered with a shadow mask. Maps data: Google ©2022 CNES, Maxar technologies. ~~Hillshade and~~ The shaded relief of map A is based on 5-m DTMs of ARPA Piemonte and regione Liguria.

420

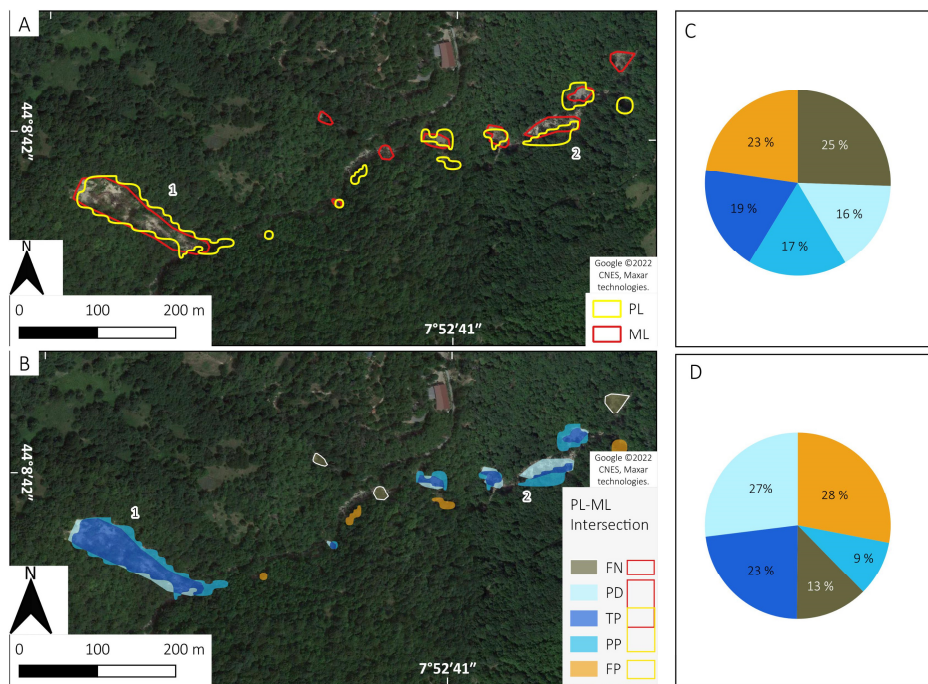
4.1.2 PL and ML comparison statistics: intersection results

The manual mapping of landslides made on post-event Google Earth and high-resolution satellite images was compared with pre-event aerial photos of 2012 and allowed the detection of 1098 ML (average density 3 ML/km²). The intersection of PL and ML datasets produced about 2620 cases.

425

The intersection of ML and PL inventories allowed the calculation of several statistics on detection capability and the evaluation of the semi-automatic detection parameters. Figure 6 A shows, over a sample area, some examples of the intersection of PL and ML inventories. In Figure 6 B, the intersections are classified into the five types of combinations defined in Table 3. In some cases, the PL/ML overlapping (TP) is almost complete (intersection 1) in Figure 6 A and B, while in other (intersection 2), TP represent a small portion of the intersection. For the whole Tanarello and Arroscia valleys case study, we also reported the intersection cases pie charts by polygons count (Figure 6 C) and total area (Figure 6 D). It is possible to note that the main difference from count to area statistics (25 % to 13 %) is for the FN case because it corresponds to many ML with a small area. In contrast, FP shows a slight increase because the size of PL is always more than 100m² (i.e. the Sentinel-2 spatial resolution).

430



435

Figure 6. Tanarello and Arroscia valleys case study. A) PL-ML inventories intersections over a sample area. B) PL-ML intersection classified by type. Pie charts of the intersection type distribution by number (C) and area (D). Maps data: Google ©2022 CNES, Maxar technologies.

440

4.1.3 PL validation statistics.

The results of the statistical analysis on detection capability and the evaluation of the semi-automatic detection parameters are shown here follow. REMOVE

Commentato [ND41]: R2: L346-347: The intersection [...] parameters --> methods not results.

445

The detailed validation results for PL made with R (see section 3.3) are shown in Figure 7. The chart of Figure 7 A shows the number distribution of TP, PP and FP cases. The TP represents about 32 % of intersected PL summed with the PP, representing 29 % of intersections, showing that the methodology correctly detects a shallow landslide in 60 % of cases.

Commentato [ND42]: L355: the methodology detects a landslide in 60% of the cases --> These TP-FP analysis results mean that the methods returns a over-representation of landslides. What about FN? Please discuss Fig 6C and 6D for this aspect as well.

450

The area frequency distribution chart (Figure 7 B) indicates that the PP cases have smaller areas (median 165 m²) than TP (230 m²) cases, this means that the TP increase up to 38 % of the case considering the area sum instead of polygons count. Several FP cases correspond to fluvial processing like bank erosion that filters could not remove. Some other regions correspond to artificial forest cuts that occurred from 2016 to 2018. In addition, the only complete summer cloud-free pair of images is august 2016 vs august 2018, and this extended period increased the probability of detecting land-use change-- not related to landslides.

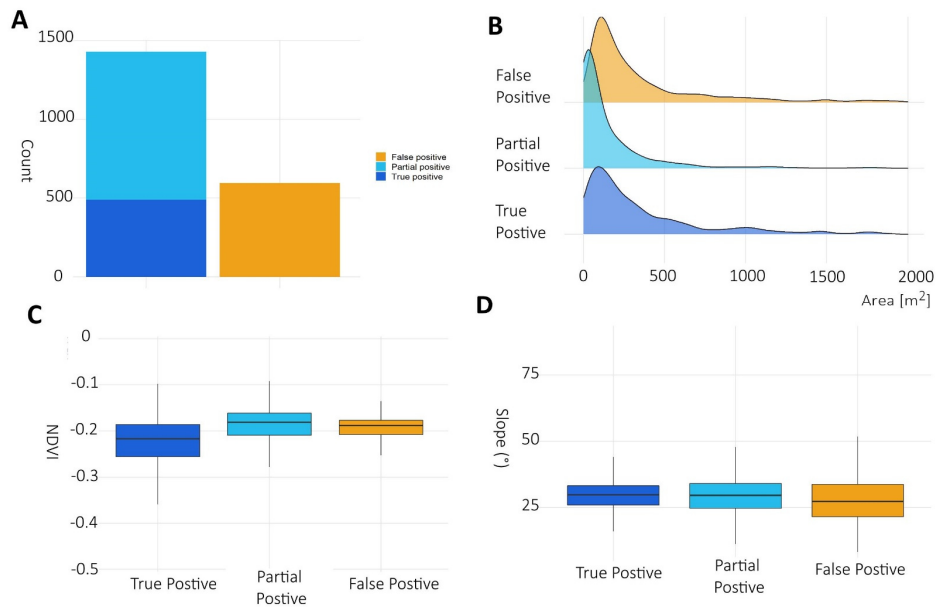
455

The NDVI_{var} and the slope are the main parameters used to detect landslides, therefore, their distribution inside the intersected PL-ML inventories helped to understand the efficiency of the semi-automatic approach. Figure 7 C shows the median NDVI_{var} for each class of ML-PL intersections. The TP cases show NDVI_{var} values below the -0.16 threshold, probably because the shallow landslides strongly impact vegetation compared to other land-use changes. Figure 7 D shows the median slope distribution, in this case, there are few differences among the classes because the slope filter (17°) removed most FP related to the slope gradient. This means that most FP cases are caused by a land-use change or riverbank erosion with the same slope gradient of shallow landslides.

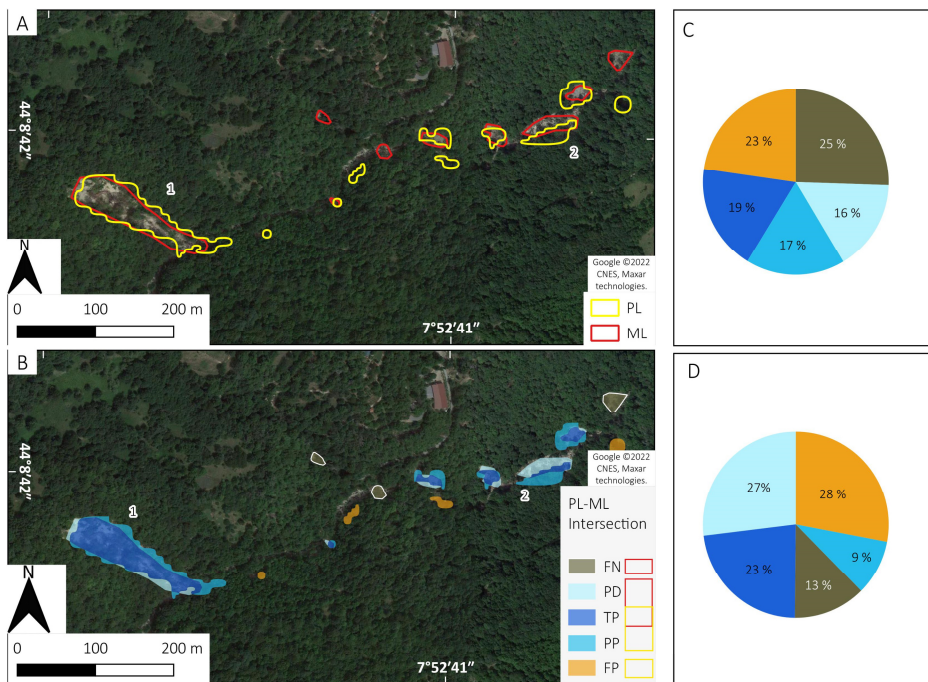
460

The FN and PD intersection cases are discussed in section 4.3.1, because they are not coming from PL and are not related to parameters used for PL methodology but to the relation of landslide size with the spatial resolution of the satellite.

465

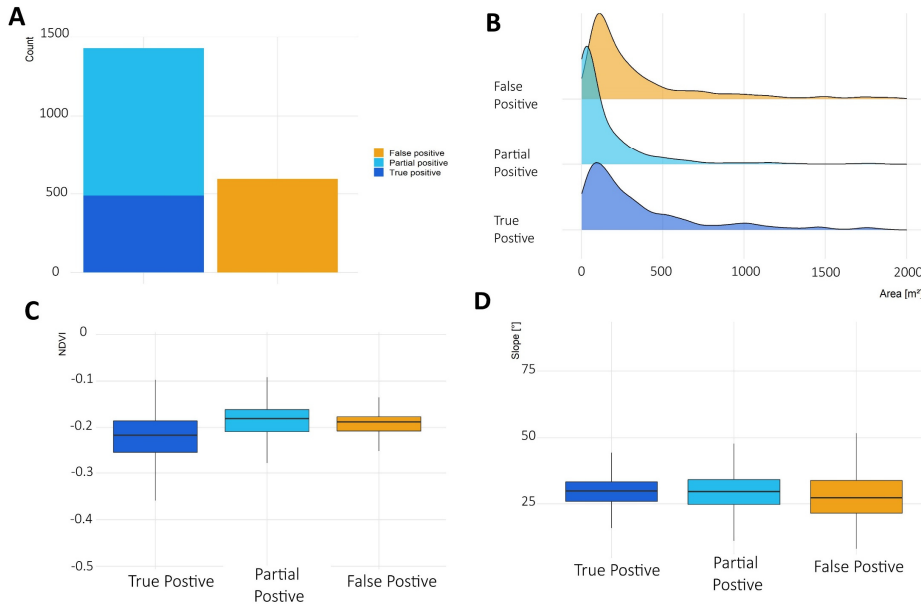


Commento [ND43]: 1.L377: Fig. 7 --> what about false negative?



470

Figure 6. Tanarello and Arroscia valleys case study. A) PL-ML inventories intersections over a sample area. B) PL-ML intersection classified by type. Pie charts of the intersection type distribution by number (C) and area (D). Maps data: Google ©2022 CNES, Maxar technologies.



475

Figure 7. PL validation statistics for the Tanarello and Arroscia valleys case study: A) Bar plot showing the number of polygons of PL classified as TP, PP and FP area; B) Area frequency distribution for the polygons classified as TP, PP, and FP area C) Box plot chart of NDVI_{var} distribution for TP, PP and FP classes ; D) Box plot chart of median slope distribution for each class of ML-PL intersection.

480

4.2 Gavi area case study.

For the Gavi area case study, we used the Sentinel-2 2019-06-20 (pre-event) and 2020-06-26 (post-event) images. The semi-automatic mapping allowed us to obtain about 3100 PL and 1077 of them are inside the training area, while about 3100 in the whole study area.

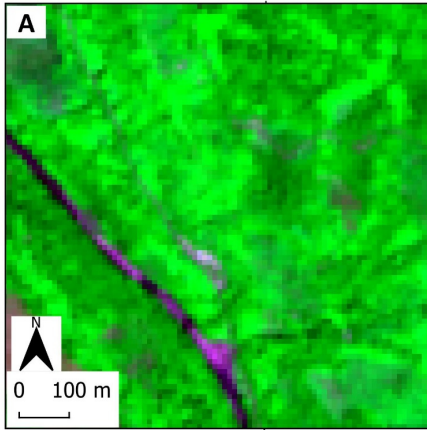
485

Figure 8 shows an example of the steps and results of our methodology over a sample area of the Gavi 2019 case study. From the comparison of pre- (Figure 8 A), and post-event images (Figure 8 B), we obtained the NDVI_{var} that was used to extrapolate the PL (Figure 8 C), which was used to extrapolate the PL. Figure 48 D compares the ML draw on high-resolution Google Earth satellite images and the PL. A detailed 3-D view from Google Earth Pro of pre- and post-event is shown in Figure 8 E and F.

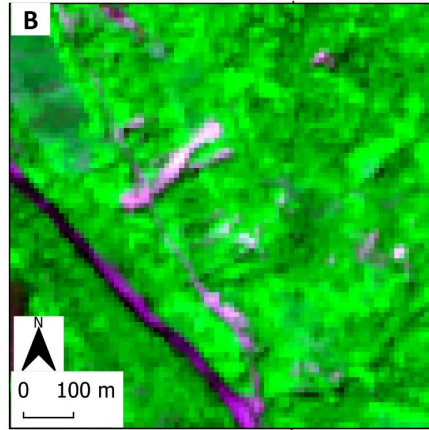
Formattato: Pedice

Commentato [ND44]: 2.L386-387: we obtained the NDVI_{var} [...] --> which was?

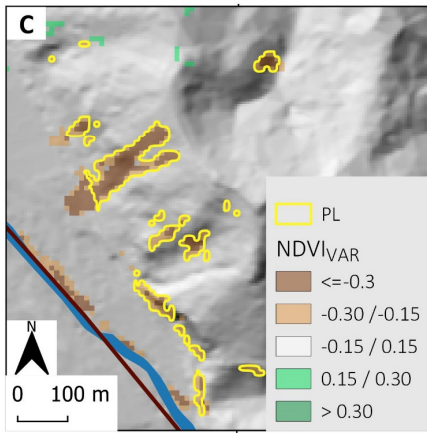
Commentato [ND45]: L387: Fig. 4D --> 8D?



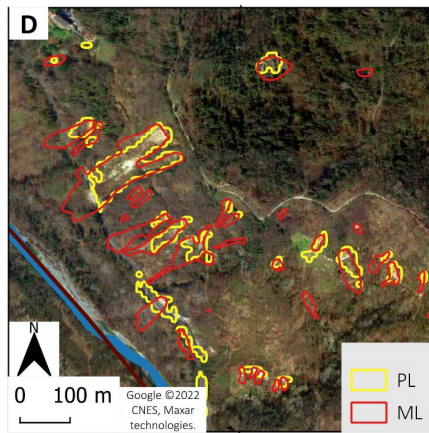
8°41'E



8°41'E



8°41'E



8°41'E



Google ©2022
CNES, Maxar
technologies.



Google ©2022
CNES, Maxar
technologies.

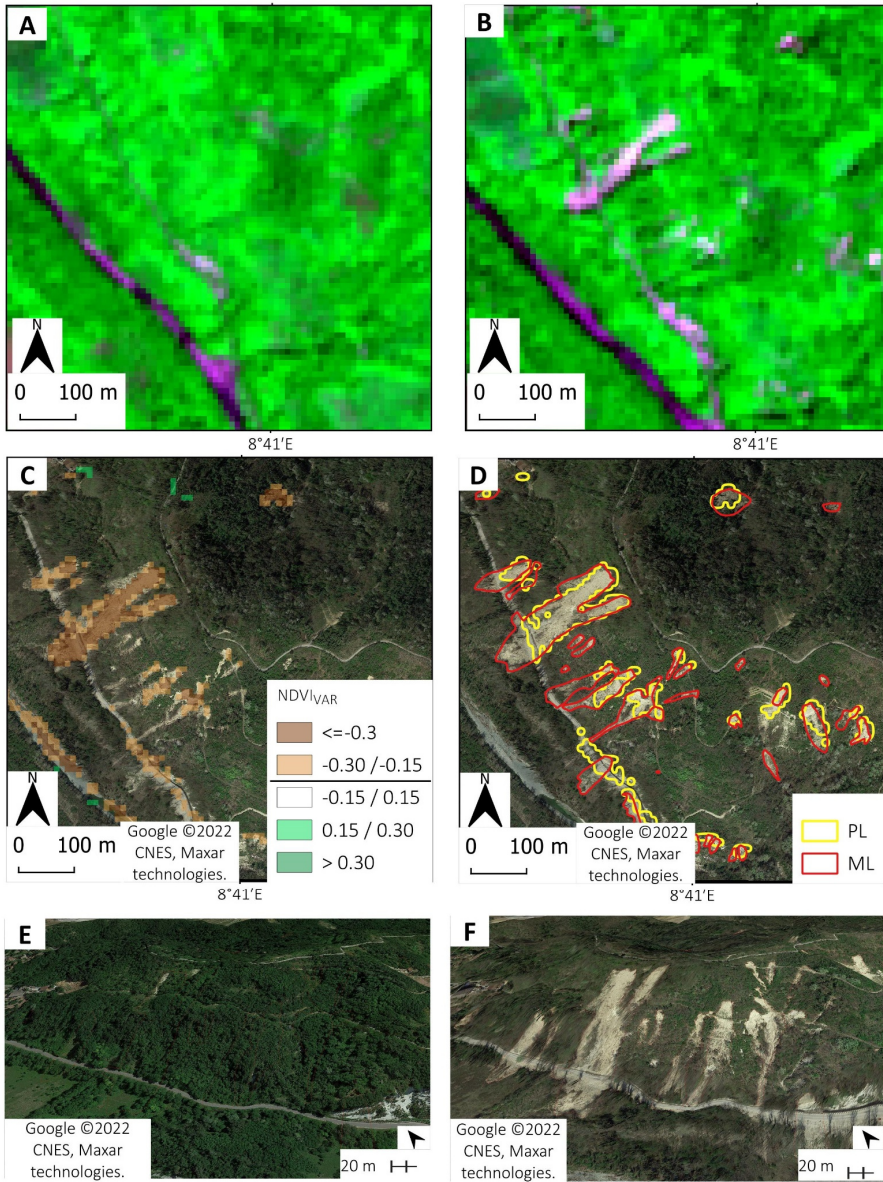
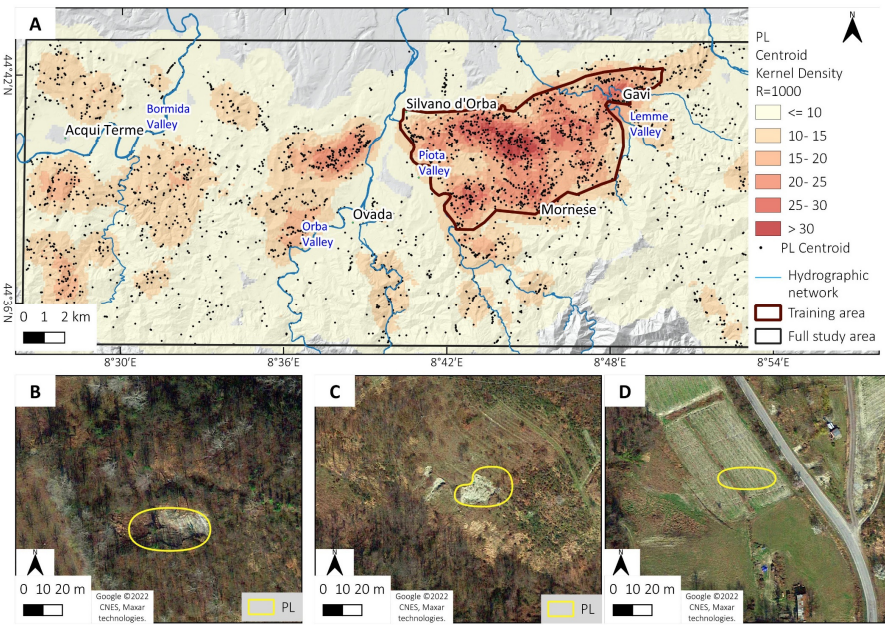


Figure 8. Example of shallow landslides detection methodology for Gavi 2019 case: A) Sentinel-2 pre-event images (RED-NIR-BLUE) acquired on 2019-06-20; B) Sentinel-2 pre-event images (RED-NIR-BLUE) acquired on 2020-06-26; C) NDVI_{var} map and PL polygons overlapped to Google-Earth post-event image; D) Comparison of ML and PL inventories overlapped to Google-Earth post-event image. Google Earth 3D view of pre- (E) and post- (F) events of the area affected by landslides. Maps data: Google ©2022 CNES, Maxar technologies.

495 **4.2.1 PL density and distribution**

Figure 9 shows the Kernel centroids density (based on a search radius of 1000 m) and distributions for PL inventory (Figure 9 A). About 3000 PLs were identified using the parameters and the filters described in the methodology section, 1100 of them are inside the training area. It is possible to detect an area of higher density chosen as to observe that the training area for manual mapping. Another area and validation area show the highest PL density. Other areas of high PL density are located North of Ovada town and other minor areas South of Acqui Terme. Here, manual mapping on HR images is proposed for further manual mapping. It is possible to analyze the different cases of PL methodology results in more detail. Figure 9 B shows the correct detection of a landslide, and its shape is almost accurate considering the Sentinel-2 resolution. Figure 9 C shows a PL that partly detected shallow landslides: in many cases, the trigger points are detected because of their abrupt changes, while the bottom part with more shallow sediment flow is not detected. It is also possible to appreciate two small shallow landslides not caught on Sentinel-2 images. Figure 9 D shows a false positive case where PL most probably detected a change in vegetation activity within a vineyard.



510 **Figure 9. October 2019 event. A) PL centroids relative Kernel Density (R=1000) over the whole AOL. Some examples of PL:**
B) PL that completely overlaps a shallow landslide; C) PL that partly overlaps a shallow landslide; D) PL that corresponds to
a false-positive case. Maps data: Google ©2022 CNES, Maxar technologies. Hillshade and The shaded relief of map A is
based on the 5-m DTM of ARPA Piemonte.

515 **4.2.2 PL and ML comparison statistics.intersection results**

Also, for the Gavi area case study, we made similar statistics on the inventories intersection used for the Tanarello and Arroscia valleys case study. The manual mapping of landslides, made on post-event Google Earth, and high-resolution

satellite images compared with pre-event aerial photos of 2018, resulted in 1178 ML (average density 23 ML/ km²).

Figure 6 The intersection of PL and ML datasets produced about 2982 cases.

520 Figure 10 A shows, over a sample area, some examples of the intersection of PL and ML inventories. In Figure 10 B, the intersections are classified into the five types of combinations (TP, FP, FN, PD and PP) defined in Table 3. In some cases, the PL/ML overlapping (TP) is almost complete (case 1) or partial (case 2). In other cases (3) the PL allowed to detect only a tiny portion of the intersection, and most of the shallow landslide area was classified as PD. For the whole 2019 study area, we also represented the intersection cases pie charts by polygons count (Figure 10 C) and area (Figure 6 D).
 525 It is possible to note that in contrast to the 2016 case, there is little difference between the count by number or total areas. The different distribution of ML size (see Figure 12 B) could explain this.

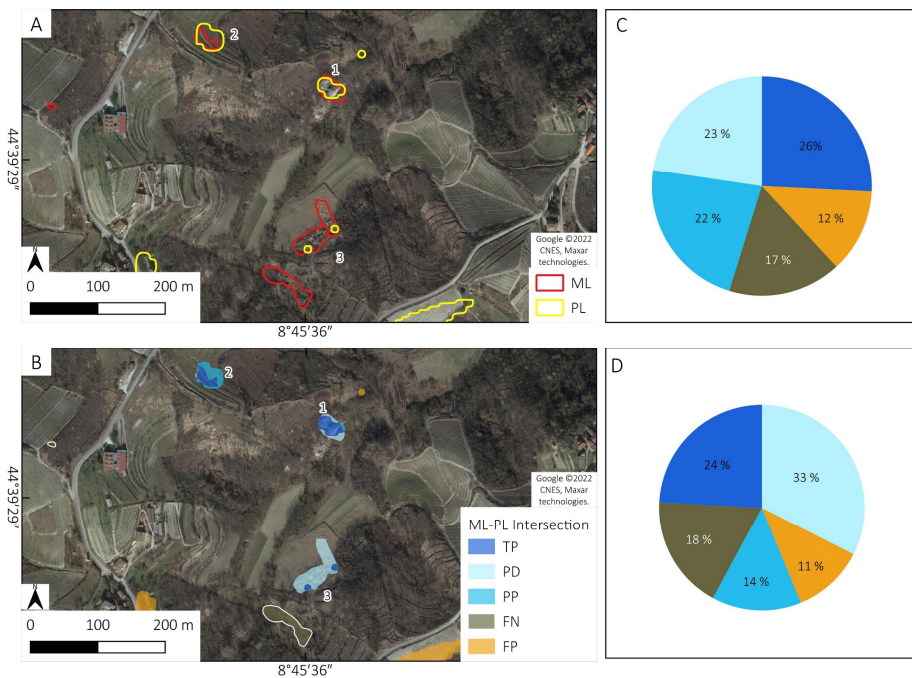


Figure 10. 2019 Gavi case study. A) PL-ML inventories intersections over a sample area. B) PL-ML intersection classified by type. Pie charts of the intersection type distribution by number (C) and area (D). Maps data: Google ©2022 CNES, Maxar technologies.

530

4.2.3 PL validation statistics.

The detailed validation statistics results for PL made with R (see section 3.3) are shown in Figure 11. The chart of Figure 11 A shows the number distribution of TP, PP and FP cases. The TP represents about 43 % of intersected PL summed with the PP, representing 37 % of cases, showing that the methodology correctly detects a shallow landslide in 80 % of

535

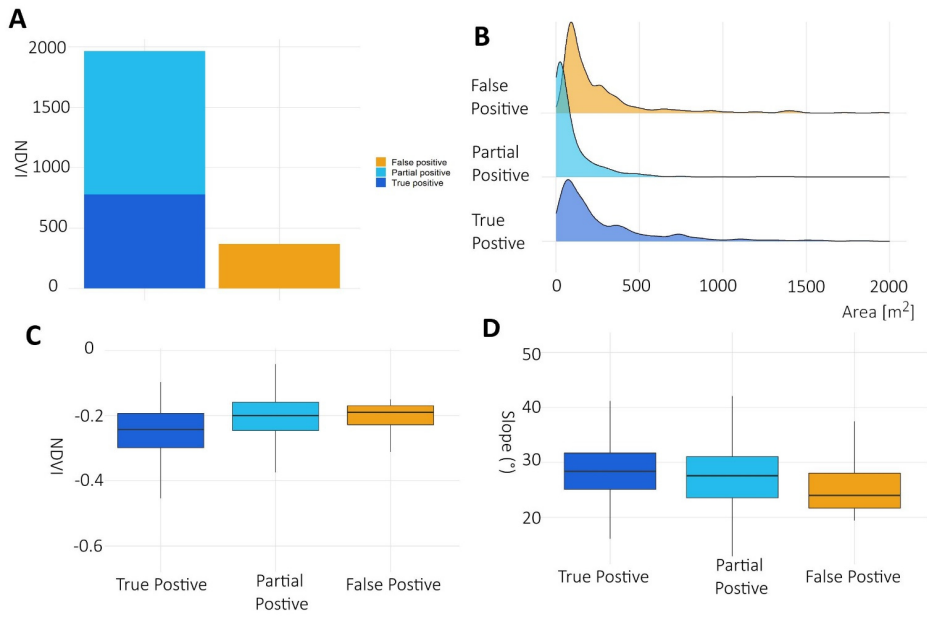
Formattato: Tipo di carattere: 10 pt
 Formattato: Normale, Giustificato, SpazioDopo: 6 pt, Interlinea: 1.5 righe

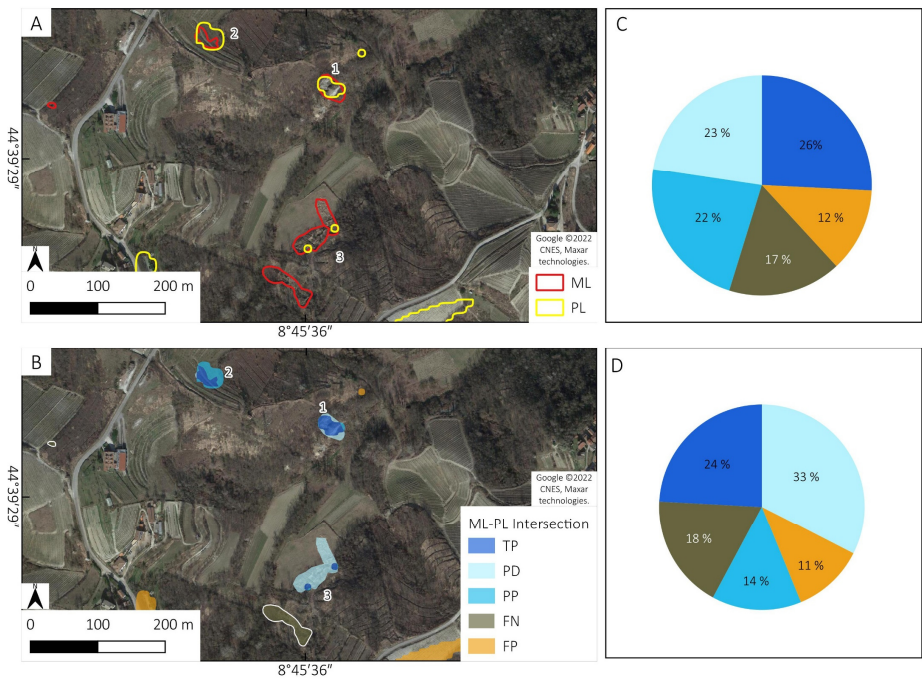
cases. The results of semi-automatic mapping for Gavi AOI are better than Arroscia-Tanarello AOI. The better performances could be explained by a better pair of pre- post- images and the stronger magnitude of the 2019 event. The area frequency distribution chart (Figure 11 B) shows that the partial positive cases have smaller areas (median 165 m²) than TP (230 m²), this implies that the percentage of TP rise from 43% to 49 % of PL considering the area sum instead of polygons count. FP cases generally correspond to changes in agriculture activity in the vineyard that occurred in 2019-2020. As previously stated, NDVI_{var} and slope were analysed in terms of intersection class and provided the same insight concerning the influence of vegetation health and acclivity.

540

[As mentioned in the Tanarello and Arroscia case study \(section 4.1.3\), The FN and PD intersection cases are discussed in section 4.3.1](#)

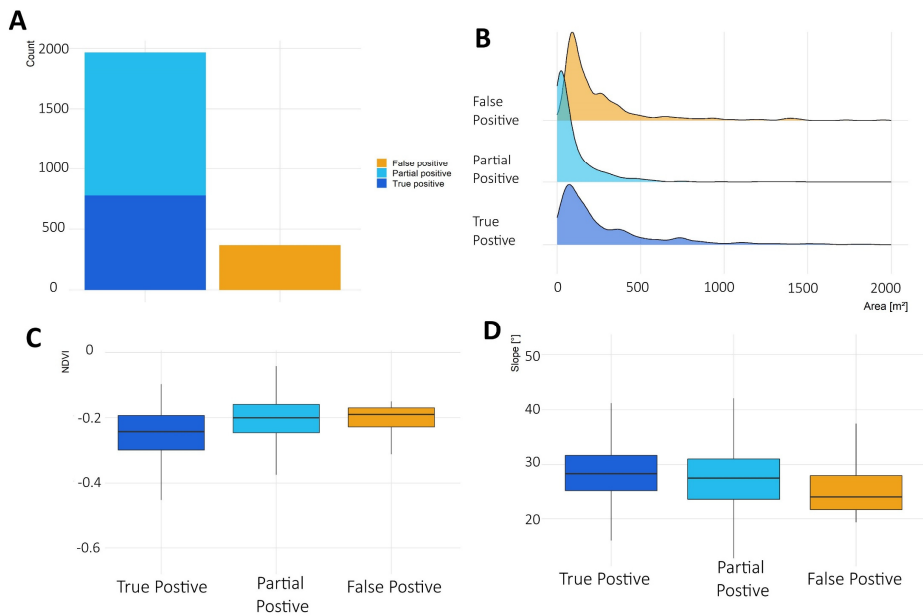
545





550

Figure 10. 2019 Gavi case study. A) PL-ML inventories intersections over a sample area. B) PL-ML intersection classified by type. Pie charts of the intersection type distribution by number (C) and area (D). Maps data: Google ©2022 CNES, Maxar technologies.



555 **Figure 11. PL validation statistics for the 2019 Gavi study area: A) Bar plot showing the number of polygons of PL classified as TP, PP and FP area; B) Area frequency distribution for the polygons classified as TP, PP, and FP area C) Box plot chart of NDVIvar distribution for TP, PP and FP classes ; D) Box plot chart of median slope distribution for each class of ML-PL intersection.**

560 **4.3. Factor that influences shallow landslides detection and false positivepositives.**

In this chapter, we discuss the main factors that, according to our results, influence the efficiency of the proposed PL methodology. As already treated in the literature, the landslide size (Bellugi et al., 2021; Fiorucci et al., 2018), land use (Mondini et al., 2011) and the temporal interval (Lindsay et al., 2022; Scheip and Wegmann, 2021) used in the pre- post-event calculation seem the most interesting to discuss on the base of our results.

565

4.3.1 Shallow landslide size, density and distributions.

The detection capacity is mainly related to shallow landslides size and spatial resolution of Sentinel-2.

570

Figure 12 A and B show the histogram distribution of ML size for the Tanarello and Arroscia valleys and Gavi study areas, respectively. ML size distribution agrees with the classical power-law distribution of shallow landslides (Bellugi et al., 2021; Guzzetti et al., 2002) for both cases study. This means that the shallow landslides smaller than 500 m² are about 60% of all ML inventories, but they represent only 20 % of the total area affected. The histograms also show that for the Tanarello and Arroscia valleys (Figure 12 A), the MLs are generally smaller than in the Gavi area. The parts of the bars red barcoloured show the ML intersected by PL (TP+PD intersection cases), it is possible to note that the lack of distribution of small landslides, in agreement (100 m²) are underestimated by PL, while for large landslides, PL

Commentato [ND46]: R2 L454: it is possible to note [...] small landslides --> unclear.

575 almost fit the ML. These results agree with the area frequency distribution for TP and PD cases shown in the Figure 7 B and Figure 11 B.

Figure 12 C and D show the DR calculated with equation 2 for the Tanarello and Arroscia valleys and Gavi study areas. The DR increases with the size of the landslides, and it is strictly related to the pixel size of Sentinel-2. For the landslides smaller than 100 m² (Sentinel-2 spatial resolution) the DR range from 10% of Tanarello and Arroscia Valley (Figure 12 C) to 15 % in the Gavi area (Figure 12 D). It is clear that for these landslides, the Sentinel-2 platform is not the optimal choice (Fiorucci et al., 2018), and manual mapping on high-resolution images is better than semi-automatic mapping. On the other hand, for the ML in the class area (500 – 1000, i.e., 5 – 10 pixels of a Sentinel-2 image), the DR range from 65 % of Tanarello and Arroscia Valley to 80 % of the Gavi area.

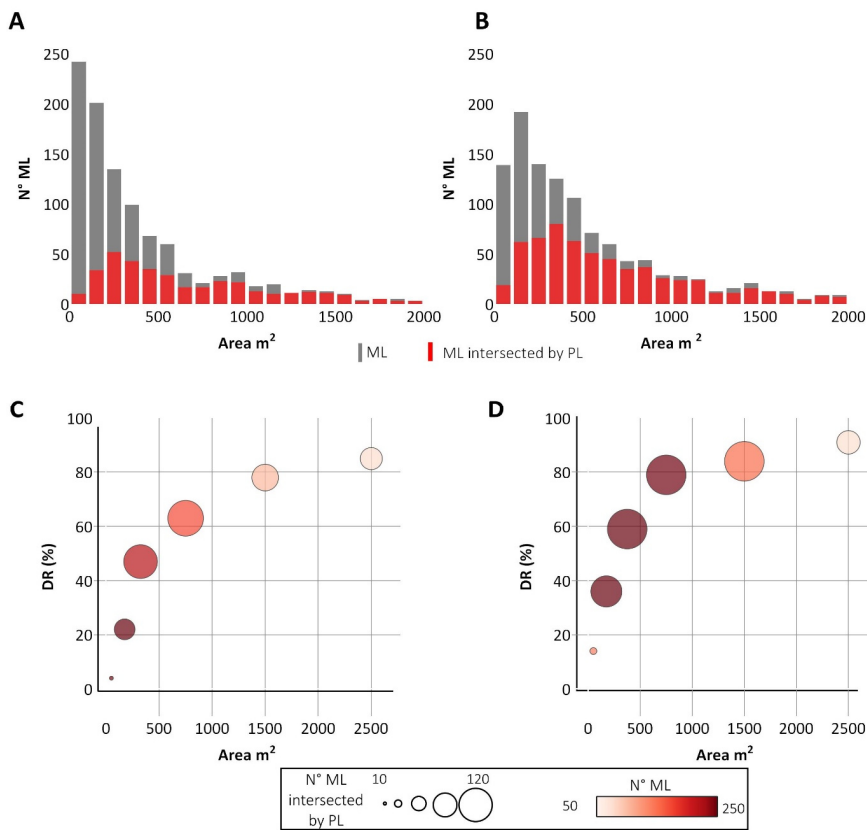
585 The overall DR considering polygons count is 39 % for the Tanarello and Arroscia Valley and 58 % for the Gavi case study, while considering the area sum, the DR is 60 % and 75%, respectively. The Gavi case study's better performance is likely related to the size distribution of shallow landslides and the better pair of images used to create PL.

590 The performance metrics Precision (P) $P = TP / (TP + FP)$, Recall $R = TP / (TP + FN)$ and F1-Score $F1 = 2TP / (2TP + FP + FN)$ without considering the intersection cases are reported in Table 4. The overall performance of our methodology is comparable with other studies, especially those using middle-resolution images (Ghorbanzadeh et al., 2021; Mondini et al., 2011; Handwerger et al., 2022). A recent study (Ganerød et al., 2023) using Sentinel-2 shows different performances depending on the study area in Norway; the best is from the deep-learning approach with a U-net architecture. Using high-resolution Planet images (Bhuyan et al., 2023) achieves high performance over several study areas. However, we assume that the different study/training/validation settings, the image used, and the event type made this comparison relative.

595 **Table 4. performance metrics of this methodology.**

AOI	P	R	F1
Arroscia / Tanarello 2016	45 %	64 %	0.529
Gavi 2019	69 %	57 %	0.623

Commentato [ND47]: R2: Results should be discussed against previous literature with major detail.



600 **Figure 12** Histogram of ML area distribution for Tanarello and Arroscia valleys (A) and Gavi (B) study areas, the grey bars represent the entire ML inventory while the red one represents the ML intersected by a PL. Detection rate (DR) for each area class for Tanarello and Arroscia valleys (C) and Gavi area (D) case study. The size of the circle is correlated with the number of detected ML; the colour scale represents the total number of ML for each class.

605 The ML and PL density and distribution comparison agree with both the Both in Tanarello and Arroscia valleys and Gavi area case studies. However, the differences described in areas, the results of spatial correlation of ML and PL density show a good agreement (Figure 13), a further confirmation of the efficiency of the previous sections evidence that PL methodology performed better in the Gavi case study.

610 The results are also evident by comparing the distribution and density of PL and ML datasets. In Specifically, in the case of 2019, both ML and PL inventories, Figure 13 A and B, show a higher density in the northern sector of the study area and a lower density in the central region. Figure 13 C shows the scatterplot between the PL and ML density, the correlation coefficient (Benesty et al., 2009) has a value of 0.85 with an $R^2 = 0.73$ using a grid of 1000 m. Moreover, the average ML density is about 23 ML/km² higher than the 2016 event (3.1 ML/km²). The difference is probably related to the more intense rainfall of October 2019 (up to 500 mm in 24 h) compared to the 2016 case (700 mm in five days).

Commentato [ND48]: R2 L476-477: The ML and PL [...] case studies --> unclear, agree with each other?

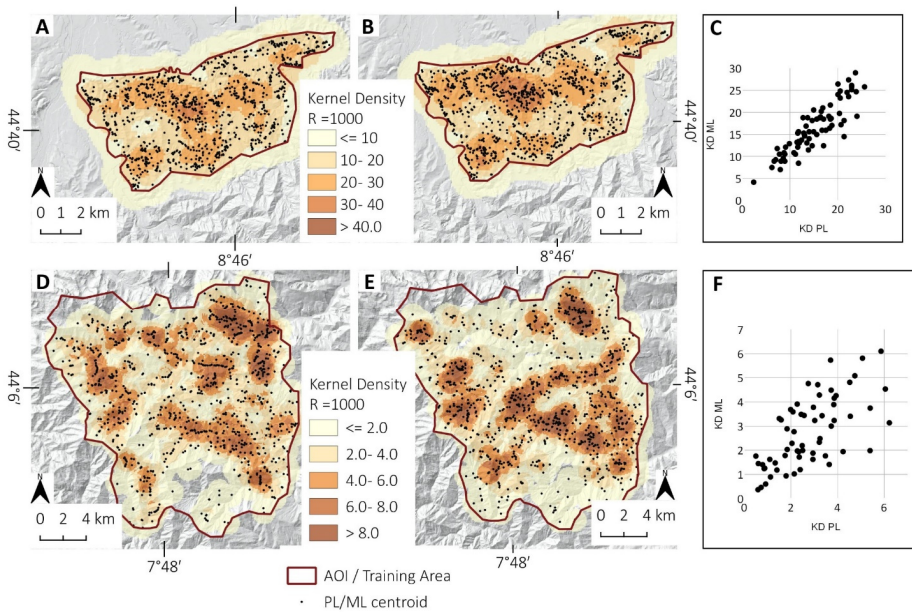
Commentato [ND49]: L479-489: whole paragraph --> These results are sort of calibration results (training and application areas are the same), correct? What if you apply the method outside the training area? This relates to my first general comment.

615

We also manually checked on Google Earth and noticed the same performance in a small validation area outside the Gavi training area.

620

In the case of 2016, there are some more discrepancies. It is possible to appreciate a higher density of PL in the NE sector (Figure 13 D). At the same time, ML shows a density peak in the Arroscia valley (Figure 13 E). Both datasets show that centroids' high density is located in the central sector, particularly in the Arroscia, Armetta and Tanarello valleys, where the density reaches a peak of 10 centroids/km². At the basin scale, PL/ML regressions show a correlation coefficient of 0.68 with an R²= 0.47 using a grid of 2500 m (Figure 13 F).



625

Figure 13. Heatmap Kernel Density for: A) Gavi PL inventory; B) Gavi ML inventory; D) Tanarello and Arroscia valleys PL inventory; E) Tanarello and Arroscia valleys ML inventory. Scatter plot of ML/PL Kernel density comparison for: C) Gavi training area; F) Tanarello and Arroscia valleys study area. Hillshade and Shaded relief of maps A, B, D and E based on 5-m DTMs of ARPA Piemonte and regione Liguria.

Commentato [ND50]: (6) Fig. 13, there is no 'C' in the caption. Also, comment on how C is created. From A and B, it seems that the kernel density points/locations are slightly different.

4.3.2 The effect of land use on PL methodology efficiency.

We deeply investigate the role of land use on landslides in landslide detection. The semi-automatic detection performed well for naturally vegetated slopes, while the detection capability decreased for cultivated landscapes.

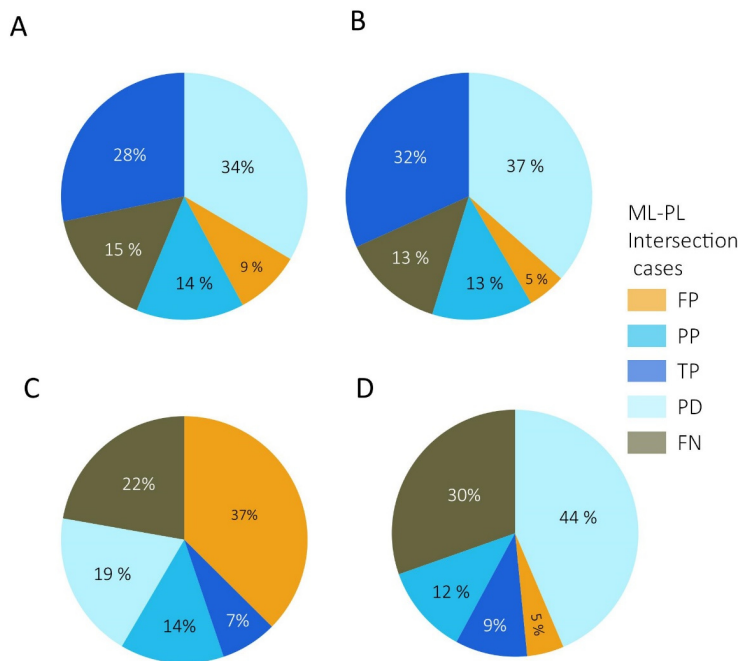
630

For instance, the statistics on intersection cases for the four main four land-use classes (Land Cover Piemonte, 2022) made for the 2019 case study allowed us to understand the variable regarding the land-use efficiency of semi-automatic mapping.

635

The forest and the new forested shrub areas (Figure 14 A and B) show a high percentage of TP cases, and about 80 % of PL correspond to shallow landslides. Here, human disturbances are limited, and most NDVI_{var} are related to landslides. The FN (15% of the area) fits small landslides not detectable with Sentinel-2 because of its spatial resolution.

The vineyard land use (Figure 14 C) shows a high FP percentage (37%). In this land use, most FP cases are changes related to vineyard management. FN are also higher (22%) compared to the forested areas. The cultivated land (Figure 14 D) shows a high percentage of FN (30%). The underestimation can be explained by smaller landslide dimensions and the agricultural practice that erases the signs of landslides.



640 **Figure 14. Gavi 2019 case study, PL-ML intersection distribution for the main land-use classes: A) Broad-Leaf forest; B) New-forest or shrubland; C) Vineyard; D) Cultivated land**

645 4.3.3 NDVI time series based on GEE

Figure 15 A and B show the NDVI time series based on Sentinel-2 computed on GEE (see data availability sections). The NDVI time series of the area affected by shallow landslides (red line in Figure 15) is based on averaged NDVI of a subset of ML polygons with an area of at least 500 m². This time series is compared with the averaged time series of averaged over a region not affected by landslides (black line in Figure 15).

650 In the case of the Arroscia-Tanarello 2016 study area (Figure 15 A), it is possible to observe that in the areas not affected by landslides, the NDVI has a relatively constant seasonal trend during 2015-2021, ranging from 0.25 in winter to 0.75 in summer. On the contrary, the areas affected by shallow landslides showed a substantial decrease of NDVI (from 0.75 to 0.4) in the post-event 2017 summer. The NDVI slowly increased during the following years, up to the value of 0.55 in 2021. If we compare the pair images (2016-08-23, 2016-08-28) used to extract the PL, we can observe an average NDVI_{var}

655 of -0.2. Unfortunately, the summer 2017 images that show the best $NDVI_{var}$, are not fully cloud-free or acquired in the same seasonal period.

In the case of the Gavi case study (Figure 15B), in those areas not affected by landslides, the NDVI has a constant seasonal trend during the period 2016-2021, ranging from 0.2 in winter to 0.8 in summer. ~~On the contrary~~In contrast, the NDVI of the ~~are~~areas affected by shallow landslides shows a substantial decrease ~~down to~~, showing a value of 0.6 ~~from~~(-0.2 variation) in the 2020 summer ~~of 2020~~. The NDVI value ~~rebound~~rebounded to 0.65 in 2021. The pair images (2019-06-26, 2020-06-20) used to extract the PL show an average $NDVI_{var}$ of -0.15. The vegetation seems to recover faster compared to the 2016 case.

The effects of land use on detection capabilities are difficult to solve with simple filters, a partial solution could be the NDVI time series analysis. The analysis of the single-pixel time series of NDVI, generated with the GEE QGIS plugin (GEE Timeseries Explorer), allowed us to understand better the effect of landslide size and land use in the capacity 665 detection of Sentinel-2, the main results are resumed in Figure 16.

Figure 16 A and A' show the location and the comparison of two NDVI time series in a broadleaf forest land use: the 1-p is entirely inside a ML of approximately 1500 m², while the 2-p is an undisturbed area. The two time series show almost the same seasonal trend until the 2019 event, after this, the NDVI of 1-p shows values of 0.2 less than the NDVI of 2-p 670 in the 2020 summer.

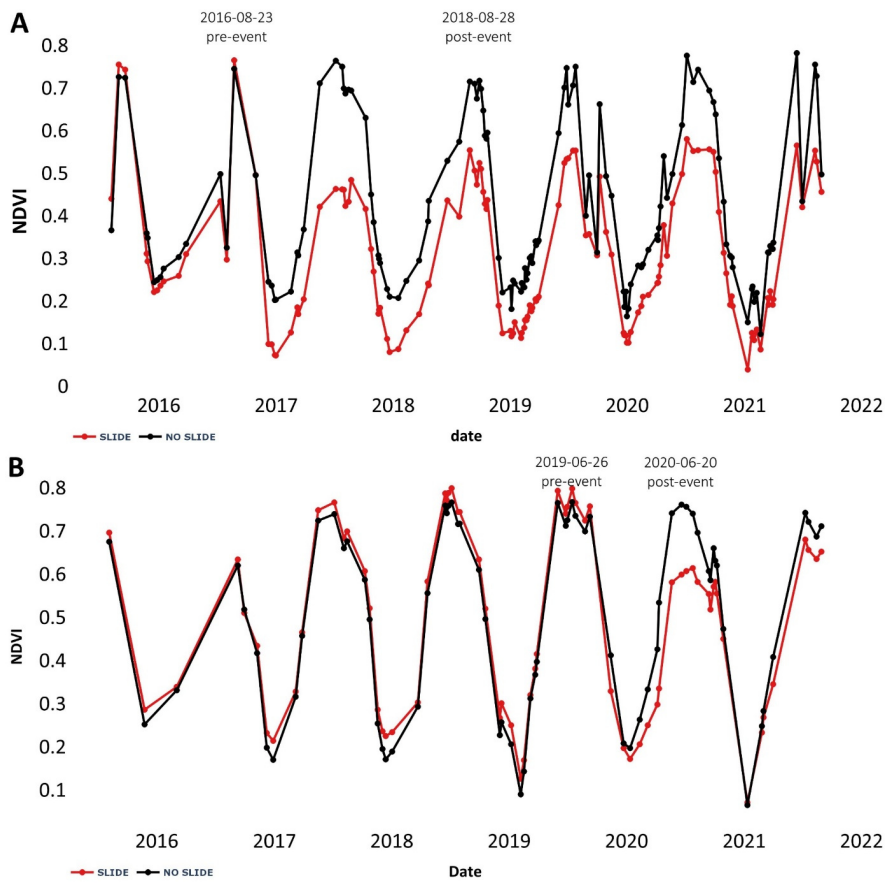
Figure 16 B and B' show the location and the comparison for two single-pixel time series located in a vineyard land use. In this case, the (5-p) is situated in ML with an approximate size of 500 m² not detected by PL methodology (a false negative case). Both slide (5-p) and no-slide (6-p) NDVI time series show an irregular trend, probably related to the agricultural activity inside the vineyard. The post-event time series shows lower NDVI values for the pixel inside the ML, 675 however, the noise is too high to extract a clear trend.

Figure 16 C and C' show the location and NDVI time series of a false-positive PL in a vineyard land use (9-p). In this case, the agricultural activity inside the vineyard caused a $NDVI_{var} < -0.16$ using the pre- and post-event pair images. However, if we look at the whole time series, there is no trace of the effect of shallow landslides.

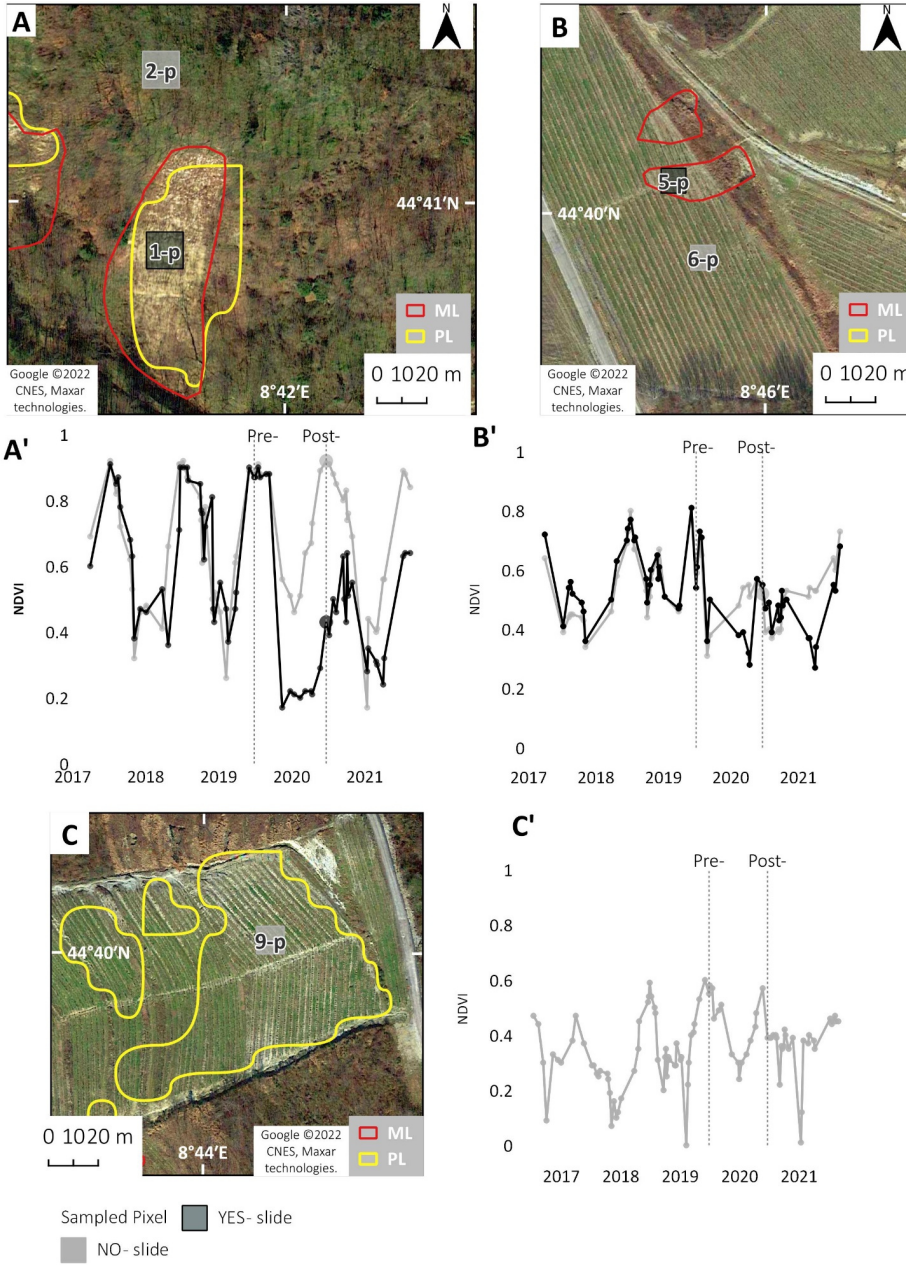
Instead of considering single pre (2019-06-26) and post (2020-06-20) event dates, the noise could be reduced if we use averaged the pre- and post-event summer (May-September) images. Multi-temporal averaged satellite data on GEE have 680 ~~been~~ already been used to improve landslide detection (Lindsay et al., 2022). For instance, using this approach, the FP of Figure 16 C disappears because the $NDVI_{var}$ is -0.16 for single pairs while it is -0.03 for the averaged summer periods.

The summer averaged pre- and post-event NDVI computed with GEE for the Gavi area are available in the data availability sections.

685



690 **Figure 15.** NDVI Time series based on Sentinel-2 data and processed with GEE: the 'Slides' red lines are the averaged time series of the selected ML; the 'no slides' black lines are the time series of the surrounding unaffected areas. A) 2016 Arrocia-Tanarello case study; B) 2019 Gavi case study.



695 **Figure 16.** NDVI Time series (2017-2021) of five sample points (Landslide / No Landslide) in the area affected by the 2019 event. A and A' comparison located in a broadleaf forest (true positive); B and B' vineyard (false negative); C and C' vineyard (false positive). The Google Earth satellite image was acquired on 2021-03-16. Maps data: Google ©2022 CNES, Maxar technologies.

6. Conclusions

A low-cost semi-automatic methodology to detect shallow landslides using cost-free data from Sentinel-2 satellites, was implemented and tested in exemplary cases. The implemented user-friendly processing is aimed to be used by a wide range of final users, such as technicians or natural hazard planners with low expertise in remote sensing processing and computer science. Landslide data and GEE scripts were also available in the free storage database for the researcher and community users. We tested the methodology on two extreme rainfall events that affected NW Italy in November 2016 (Tanarello and Arroscia valleys) and October 2019 (Gavi area).

We obtain a polygons dataset representing potential landslides (PL) and their density maps with the semi-automatic mapping. The PL density maps aim to identify the most affected areas, where to focus the manual mapping on high-resolution images. The PL dataset is created on three steps approach: i) choice of the best pair of Sentinel-2 images also with the help of NDVI time series computed with Google Earth Engine (GEE); ii) creation NDVI_{VAR} map from pre- and post-event images, iii) geomorphological filters based on slope and others parameters such as distance from the hydrographic network, iv) eventual re-calibration of PL parameters with landslides manually detected (ML). In the study areas of Tanarello and Arroscia Valley, and Gavi, 1077 and 2576 PL were detected, respectively, and their. The areas with the highest PL density matches also match with most affected areas by rainfall events.

The dataset obtained PL inventory was compared with manual mapping based on high-resolution images on training and validation areas. We manually map landslides on the free-cost high-resolution images (e.g., Google Earth, national or regional cartographic services). The manual mapping detected about 1100 ML over 300 km² in the Tanarello and Arroscia valleys and about 1180 ML over 55 km² in the Gavi area. The PL datasets were then compared with landslides manually (ML). The ML and PL inventories comparison shows a good agreement in density and distributions, especially for the Gavi case study.

The results show that according to the findings, the semi-automatic approach identifies method can detect the majority (≈ about 60 %) of shallow landslides larger than 2/3 two or three times the size of Sentinel-2 ground pixel size pixels (100 m²), while. In contrast, the PL method can identify only 20% of small landslides (≤ less than 100 m²) are detected in size. In agreement with the power-law, small landslides are a high number, but a small fraction of the affected area. Consequently, the false-negative represents 60 % to 40 % of the cases but only 20-25 % of the area affected. In the future, using high-resolution cost-free satellite images for semi-automatic methods could drastically increase the detection capacity. Land use is another factor that influences detection capacity: in the Gavi study area, the detection rate reached 73 % on natural vegetation like forest land use, while in cultivated areas, DR decreased up to 41 %.

The false-positive rate (FPR) (28 % for the Gavi area and 48% for Tanarello and Arroscia valley) is related to riverbank erosions or artificial change in vegetation pattern that was impossible to remove with geomorphological filters. Also, for FPR, the land use drives the performance: it ranges from 45 % of the vineyard to 20 % of the forest

The analysis of the NDVI time series with GEE was proper to identify the best pair of images and monitor the behaviour of vegetation of affected areas. For the middle latitudes, the best comparison is within the period of maximum vegetation activity (e.g., summer images for middle latitude). The time series showed a progressive vegetation recovery throughout the years, decreasing the detection capacity of this approach. The time-series analysis also suggested that an averaged NDVI of summer periods could reduce the effect of agricultural changes on vegetation and limit the false positive. The evidence indicated that multi-temporal analysis needs to be developed to improve semi-automatic mapping efficiency, which could be the key to future studies.

Commentato [ND51]: R2 L578: their density matches [...] rainfall events --> unclear.:

Commentato [ND52]: L582: landslides manually --> landslides manually detected?

Commentato [ND53]: R2: L583: good agreement --> I believe it is worth mentioning that some parameters of the automatic recognition needed calibration.

Commentato [ND54]: R2: L584-585: whole sentence --> unclear, >60% of landslides with areas larger than 67 m² (2/3 of 100 m²) but <20% for landslides smaller than 100 m²?

Commentato [ND55]: L595: for middle latitudes, the best comparison is with summer images --> This was an assumption in selecting the images (only June-September), I suggest not to present it as a conclusion.

Data availability

ML and PL datasets used in this study are available in KML format on the Zenodo platform (Notti et al., 2022)

740 The Google Earth Engine scripts used for this paper are:

- NDVI Time series of some sampled areas to select the best pair of images for the PL creation (Tanarello and Arroscia Valleys and GAVI AOIs (Fig. 15 of the manuscript) <https://code.earthengine.google.com/8f4d08db4d34099bb1a4cd1fd15bf05b?noload=true>
- Sampled NDVI Time series from different intersection cases for Tanarello and Arroscia Valleys study area <https://code.earthengine.google.com/47e5883e0fe7beae589df4c42421dd3b?noload=true>
- Sampled NDVI Time series from some test areas over the Gavi study area <https://code.earthengine.google.com/e97fd46102cca3ee25b441a8ebff8400?noload=true>
- Multi-temporal averaged ~~pre—and—post-event—~~NDVI \overline{NDVI}_{var} for the whole Gavi study area <https://code.earthengine.google.com/f773ed58fe39e201261e5e13b4275f97?noload=true><https://code.earthengine.google.com/454fd113a211fb8b745f5aa658da234c?noload=true>

750

The Sentinel-2 images were downloaded from Copernicus ESA open-access hub website: <https://scihub.copernicus.eu/>

The High-resolution images were uploaded in QGIS as WMS layers from the following link:

- Google Earth Satellite layers, XYZ tiles for QGIS: <http://mt0.google.com/vt/lyrs=s&hl=en&x={x}&y={y}&z={z}>
- The 2012 Orthophots that cover both study areas are available on the national cartographic service (PCN) WMS: <http://www.pcn.minambiente.it/mattm/servizio-wms/> Accessed: 2022-04-20
- The Piemonte region 2018 orthophoto is available on the following WMS: https://opengis.csi.it/mp/regp_agea_2018?service=WMS&request=GetCapabilities&version=1.3.0. The Regione Liguria 2016 Orthophoto are available on <http://www.cartografiarl.regione.liguria.it/mapserver/4.10/mapserv.exe?MAP=E:/Progetti/mapfiles/repertoriocartografico/ORTOFOTO/1828.map&VERSION=1.3> Accessed: 2022-04-20

760

DTM data can be ~~download~~downloaded from Regione Piemonte and Liguria geo-portal:

- https://www.geoportale.piemonte.it/geonetwork/srv/api/records/r_piemon:224de2ac-023e-441c-9ae0-ea493b217a8e Accessed: 2022-06-30
- <https://srvcarto.regione.liguria.it/geoviewer2/pages/apps/geoportale/index.html?id=2056> Italian) Accessed: 2022-06-30

765

~~The software~~ Google Earth Pro ~~software~~ was also used to map and check inventories at high resolution.

Other data, such as land use, NDVI elaborations and meteorological data, can be obtained from the first/corresponding author upon reasonable request.

770 **Acknowledgements**

[This work was supported by Major International (Regional) Joint Research Project of NSFC (No. 42020104006)]

Commentato [ND56]: frase

Author contribution.

775 Planning and conceptualization were done by DN. Responsible for data curation were DN, MC, and DGo. The mapping was done by DN and MC. The statistical analyses were performed by DGo. The original manuscript was written by DN. MC, DGo and DGi were involved in reviewing and editing of the manuscript. Supervision and funding acquisition were provided by DGi.

Reference

- ARPA Piemonte: Gli eventi alluvionali in Piemonte - Evento del 21-25 novembre 2016, Turin, 2018.
- 780 Bellugi, D. G., Milledge David G., Cuffey Kurt M., Dietrich William E., and Larsen Laurel G.: Controls on the size distributions of shallow landslides, *Proceedings of the National Academy of Sciences*, 118, e2021855118, <https://doi.org/10.1073/pnas.2021855118>, 2021.
- Benesty, J., Chen, J., Huang, Y., and Cohen, I.: Pearson Correlation Coefficient, in: *Noise Reduction in Speech Processing*, edited by: Cohen, I., Huang, Y., Chen, J., and Benesty, J., Springer Berlin Heidelberg, Berlin, Heidelberg, 1–4, https://doi.org/10.1007/978-3-642-00296-0_5, 2009.
- 785 [Bhuyan, K., Tanyaş, H., Nava, L., Puliero, S., Meena, S. R., Floris, M., van Westen, C., and Catani, F.: Generating multi-temporal landslide inventories through a general deep transfer learning strategy using HR EO data, *Scientific Reports*, 13, 162, <https://doi.org/10.1038/s41598-022-27352-y>, 2023.](#)
- Bordoni, M., Meisina, C., Valentino, R., Lu, N., Bittelli, M., and Chersich, S.: Hydrological factors affecting rainfall-induced shallow landslides: from the field monitoring to a simplified slope stability analysis, [Engineering Geology](#), 193, 19–37, <https://doi.org/10.1016/j.enggeo.2015.04.006>, 2015.
- 790 [Borrelli, L., Cofone, G., Coscarelli, R., and Gullà, G.: Shallow landslides triggered by consecutive rainfall events at Catanzaro strait \(Calabria–Southern Italy\), *Journal of Maps*, 11, 730–744, <https://doi.org/10.1080/17445647.2014.943814>, 2015.](#)
- 795 [Caine, N.: The rainfall intensity-duration control of shallow landslides and debris flows, *Geografiska annaler: series A, physical geography*, 62, 23–27, 1980.](#)
- Cardinali, M., Ardizzone, F., Galli, M., Guzzetti, F., and Reichenbach, P.: Landslides triggered by rapid snow melting: the December 1996–January 1997 event in Central Italy, in: *Proceedings 1st Plinius Conference on Mediterranean Storms*, 439–448, 2000.

- 800 Carrara, A.: Uncertainty in Evaluating Landslide Hazard and Risk, in: Prediction and Perception of Natural Hazards: Proceedings Symposium, 22–26 October 1990, Perugia, Italy, edited by: Nemeč, J., Nigg, J. M., and Siccardi, F., Springer Netherlands, Dordrecht, 101–109, https://doi.org/10.1007/978-94-015-8190-5_12, 1993.
- Nimbus Web Eventi Meteorologici: <http://www.nimbus.it/eventi/2016/161125AlluvioniNordOvest.htm>, last access: 10 June 2022.
- 805 Catani, F.: Landslide detection by deep learning of non-nadir and crowdsourced optical images, *Landslides*, 18, 1025–1044, 2021.
- Cevasco, A., Pepe, G., and Brandolini, P.: The influences of geological and land use settings on shallow landslides triggered by an intense rainfall event in a coastal terraced environment, *Bulletin of Engineering Geology and the Environment*, 73, 859–875, <https://doi.org/10.1007/s10064-013-0544-x>, 2014.
- 810 Cignetti, M., Godone, D., and Giordan, D.: Shallow landslide susceptibility, Rupinaro catchment, Liguria (northwestern Italy), *Journal of Maps*, 1–13, <https://doi.org/10.1080/17445647.2019.1593252>, 2019.
- Conrad, O., Bechtel, B., Bock, M., Dietrich, H., Fischer, E., Gerlitz, L., Wehberg, J., Wichmann, V., and Böhner, J.: System for Automated Geoscientific Analyses (SAGA) v. 2.1.4, *Geosci. Model Dev.*, 8, 1991–2007, <https://doi.org/10.5194/gmd-8-1991-2015>, 2015.
- 815 Copernicus Climate Change Service: <https://climate.copernicus.eu/ESOTC/2019/wet-end-year-western-and-southern-europe>, last access: 29 April 2022.
- Copernicus Open Access Hub: <https://scihub.copernicus.eu/>, last access: 8 June 2022.
- Cremonini, R. and Tiranti, D.: The weather radar observations applied to shallow landslides prediction: a case study from north-western Italy, *Frontiers in Earth Science*, 6, 134, <https://doi.org/10.3389/feart.2018.00134>, 2018.
- 820 D’Amato Avanzi, G., Galanti, Y., Giannecchini, R., and Bartelletti, C.: Shallow Landslides Triggered by the 25 October 2011 Extreme Rainfall in Eastern Liguria (Italy), in: *Engineering Geology for Society and Territory - Volume 2*, edited by: Lollino, G., Giordan, D., Crosta, G. B., Corominas, J., Azzam, R., Wasowski, J., and Sciarra, N., Springer International Publishing, Cham, 515–519, 2015.
- Ferrari, F., Cassola, F., Tuju, P. E., and Mazzino, A.: RANS and LES face to face for forecasting extreme precipitation events in the Liguria region (northwestern Italy), *Atmospheric Research*, 259, 105654, <https://doi.org/10.1016/j.atmosres.2021.105654>, 2021.
- 825 Fiorucci, F., Cardinali, M., Carlà, R., Rossi, M., Mondini, A. C., Santurri, L., Ardizzone, F., and Guzzetti, F.: Seasonal landslide mapping and estimation of landslide mobilization rates using aerial and satellite images, *Geomorphology*, 129, 59–70, <https://doi.org/10.1016/j.geomorph.2011.01.013>, 2011.

- 830 Fiorucci, F., Giordan, D., Santangelo, M., Dutto, F., Rossi, M., and Guzzetti, F.: Criteria for the optimal selection of remote sensing optical images to map event landslides, *Nat. Hazards Earth Syst. Sci.*, 18, 405–417, <https://doi.org/10.5194/nhess-18-405-2018>, 2018.
- Fiorucci, F., Ardizzone, F., Mondini, A. C., Viero, A., and Guzzetti, F.: Visual interpretation of stereoscopic NDVI satellite images to map rainfall-induced landslides, *Landslides*, 16, 165–174, <https://doi.org/10.1007/s10346-018-1069-y>, 2019.
- 835 [Fратиanni, S. and Acquaoita, F.: The climate of Italy, Landscapes and landforms of Italy, 29–38, 2017.](#)
- Gallus Jr, W. A., Parodi, A., and Maugeri, M.: Possible impacts of a changing climate on intense Ligurian Sea rainfall events, *International Journal of Climatology*, 38, e323–e329, <https://doi.org/10.1002/joc.5372>, 2018.
- [Ganerød, A. J., Lindsay, E., Fredin, O., Myrvoll, T.-A., Nordal, S., and Rød, J. K.: Globally-vs Locally-trained Machine Learning Models for Land-slide Detection: A Case Study of a Glacial Landscape, Remote Sensing, 15, 895, https://doi.org/doi.org/10.3390/rs15040895, 2023.](#)
- 840 [Gariano, S. L. and Guzzetti, F.: Landslides in a changing climate, Earth-Science Reviews, 162, 227–252, https://doi.org/10.1016/j.earscirev.2016.08.011, 2016.](#)
- Ghorbanzadeh, O., Crivellari, A., Ghamisi, P., Shahabi, H., and Blaschke, T.: A comprehensive transferability evaluation of U-Net and ResU-Net for landslide detection from Sentinel-2 data (case study areas from Taiwan, China, and Japan), *Scientific Reports*, 11, 14629, <https://doi.org/10.1038/s41598-021-94190-9>, 2021.
- 845 Giordan, D., Cignetti, M., Baldo, M., and Godone, D.: Relationship between man-made environment and slope stability: the case of 2014 rainfall events in the terraced landscape of the Liguria region (northwestern Italy), *null*, 8, 1833–1852, <https://doi.org/10.1080/19475705.2017.1391129>, 2017.
- 850 Gorelick, N., Hancher, M., Dixon, M., Ilyushchenko, S., Thau, D., and Moore, R.: Google Earth Engine: Planetary-scale geospatial analysis for everyone, *Remote Sensing of Environment*, 202, 18–27, <https://doi.org/10.1016/j.rse.2017.06.031>, 2017.
- Govi, M.: Gli eventi alluvionali del 1977 in Piemonte: problemi di protezione idrogeologica, in: Proc. Conf. “Pianificazione territoriale e geologia”, Regione Piemonte–Dip. Organizzazione e gestione territorio e Assessorato Pianificazione Territorio, 37–45, 1978.
- 855 Guzzetti, F., Malamud, B. D., Turcotte, D. L., and Reichenbach, P.: Power-law correlations of landslide areas in central Italy, *Earth and Planetary Science Letters*, 195, 169–183, [https://doi.org/10.1016/S0012-821X\(01\)00589-1](https://doi.org/10.1016/S0012-821X(01)00589-1), 2002.

- 860 Guzzetti, F., Cardinali, M., Reichenbach, P., Cipolla, F., Sebastiani, C., Galli, M., and Salvati, P.: Landslides triggered
by the 23 November 2000 rainfall event in the Imperia Province, Western Liguria, Italy, *Engineering Geology*,
73, 229–245, <https://doi.org/10.1016/j.enggeo.2004.01.006>, 2004.
- Handwerger, A. L., Huang, M.-H., Jones, S. Y., Amatya, P., Kerner, H. R., and Kirschbaum, D. B.: Generating
landslide density heatmaps for rapid detection using open-access satellite radar data in Google Earth Engine,
Nat. Hazards Earth Syst. Sci., 22, 753–773, <https://doi.org/10.5194/nhess-22-753-2022>, 2022.
- 865 Hölbling, D., Friedl, B., and Eisank, C.: An object-based approach for semi-automated landslide change detection and
attribution of changes to landslide classes in northern Taiwan, *Earth Science Informatics*, 8, 327–335, 2015.
- IPCC, – Intergovernmental Panel on Climate Change: Climate Change 2014: Synthesis Report. Contribution of
Working Groups I, II and III to the Fifth Assessment Report of the Intergovernmental Panel on Climate
Change, Geneva, 2014.
- 870 Lanteaume, M., Radulescu, N., Gravos, M., Feraud, J., Faure-Muret, A., and Haccard, D.: Notice explicative, Carte
Géologique de France (1/50.000), feuille Viève-Tende (948), 1990. [Bureau de Recherches Géologiques et
Minières, Orléans, 1990.](https://www.brgm.fr/fr/productions/ouvrages/notice-explicative)
- Lindsay, E., Frauenfelder, R., Rütther, D., Nava, L., Rubensdotter, L., Strout, J., and Nordal, S.: Multi-Temporal
Satellite Image Composites in Google Earth Engine for Improved Landslide Visibility: A Case Study of a
875 Glacial Landscape, *Remote Sensing*, 14, <https://doi.org/10.3390/rs14102301>, 2022.
- Lu, P., Qin, Y., Li, Z., Mondini, A. C., and Casagli, N.: Landslide mapping from multi-sensor data through improved
change detection-based Markov random field, *Remote Sensing of Environment*, 231, 111235,
<https://doi.org/10.1016/j.rse.2019.111235>, 2019.
- Luino, F.: The flood and landslide event of November 4–6 1994 in Piedmont Region (Northwestern Italy): Causes and
880 related effects in Tanaro Valley, *Physics and Chemistry of the Earth, Part A: Solid Earth and Geodesy*, 24,
123–129, [https://doi.org/10.1016/S1464-1895\(99\)00007-1](https://doi.org/10.1016/S1464-1895(99)00007-1), 1999.
- Mandarino, A., Luino, F., and Faccini, F.: Flood-induced ground effects and flood-water dynamics for hydro-
geomorphic hazard assessment: the 21–22 October 2019 extreme flood along the lower Orba River
(Alessandria, NW Italy), *null*, 17, 136–151, <https://doi.org/10.1080/17445647.2020.1866702>, 2021.
- 885 Martha, T. R., Kerle, N., Jetten, V., van Westen, C. J., and Kumar, K. V.: Characterising spectral, spatial and
morphometric properties of landslides for semi-automatic detection using object-oriented methods,
Geomorphology, 116, 24–36, <https://doi.org/10.1016/j.geomorph.2009.10.004>, 2010.
- Meteologix: <https://meteologix.com/it/precipitation/alessandria/calibrated-precipitation-total-6h/20191021-2050z.html>,
last access: 27 May 2022.

- 890 Mohan, A., Singh, A. K., Kumar, B., and Dwivedi, R.: Review on remote sensing methods for landslide detection using machine and deep learning, *Transactions on Emerging Telecommunications Technologies*, 32, e3998, <https://doi.org/doi.org/10.1002/ett.3998>, 2021.
- Mondini, A. C., Guzzetti, F., Reichenbach, P., Rossi, M., Cardinali, M., and Ardizzone, F.: Semi-automatic recognition and mapping of rainfall induced shallow landslides using optical satellite images, *Remote Sensing of Environment*, 115, 1743–1757, <https://doi.org/10.1016/j.rse.2011.03.006>, 2011.
- 895 Nava, L., Bhuyan, K., Meena, S. R., Monserrat, O., and Catani, F.: Rapid Mapping of Landslides on SAR Data by Attention U-Net, *Remote Sensing*, 14, 1449, <https://doi.org/10.3390/rs14061449>, 2022.
- Notti, D., Giordan, D., Caló, F., Pepe, A., Zucca, F., and Galve, J.: Potential and limitations of open satellite data for flood mapping, *Remote Sensing*, 10, 1673, 2018.
- 900 Notti, D., Wrzesniak, A., Dematteis, N., Lollino, P., Fazio, N. L., Zucca, F., and Giordan, D.: A multidisciplinary investigation of deep-seated landslide reactivation triggered by an extreme rainfall event: a case study of the Monesi di Mendatica landslide, Ligurian Alps, *Landslides*, 1–25, <https://doi.org/10.1007/s10346-021-01651-3>, 2021.
- Notti, D., Cignetti, M., Godone, D., and Giordan, D.: Semi-automatic and manual shallow landslide inventories of two extreme rainfall events., <https://doi.org/10.5281/zenodo.6617194>, 2022.
- 905 Nowak, B., Marliac, G., and Michaud, A.: Estimation of winter soil cover by vegetation before spring-sown crops for mainland France using multispectral satellite imagery, *Environmental Research Letters*, 16, 064024, 2021.
- Paliaga, G. and Parodi, A.: Geo-Hydrological Events and Temporal Trends in CAPE and TCWV over the Main Cities Facing the Mediterranean Sea in the Period 1979–2018, *Atmosphere*, 13, <https://doi.org/10.3390/atmos13010089>, 2022.
- 910 Pepe, G., Piazza, M., and Cevasco, A.: Geomechanical characterization of a highly heterogeneous flysch rock mass by means of the GSI method, *Bulletin of Engineering Geology and the Environment*, 74, 465–477, <https://doi.org/10.1007/s10064-014-0642-4>, 2015.
- Pepe, G., Mandarino, A., Raso, E., Cevasco, A., Firpo, M., and Casagli, N.: Extreme Flood and Landslides Triggered in the Arroscia Valley (Liguria Region, Northwestern Italy) During the November 2016 Rainfall Event, in: *IAEG/AEG Annual Meeting Proceedings, San Francisco, California, 2018-Volume 1*, 171–175, 2019.
- 915 Piana, F., Fioraso, G., Irace, A., Mosca, P., d’Atri, A., Barale, L., Falletti, P., Monegato, G., Morelli, M., Tallone, S., and Vigna, G. B.: Geology of Piemonte region (NW Italy, Alps–Apennines interference zone), *null*, 13, 395–405, <https://doi.org/10.1080/17445647.2017.1316218>, 2017.

- 920 Prakash, N., Manconi, A., and Loew, S.: A new strategy to map landslides with a generalized convolutional neural network, *Scientific reports*, 11, 1–15, 2021.
- QGIS Association.: QGIS.org, 2022. QGIS Geographic Information System. QGIS Association., 2022.
- Qin, Y., Lu, P., and Li, Z.: LANDSLIDE INVENTORY MAPPING FROM BITEMPORAL 10 m SENTINEL-2 IMAGES USING CHANGE DETECTION BASED MARKOV RANDOM FIELD, *Int. Arch. Photogramm. Remote Sens. Spatial Inf. Sci.*, XLII–3, 1447–1452, <https://doi.org/10.5194/isprs-archives-XLII-3-1447-2018>, 2018.
- 925 R Core Team: R: A language and environment for statistical computing., [R Foundation for Statistical Computing, Vienna, Austria](https://www.R-project.org/), 2020.
- GEE Timeseries Explorer: <https://geetimeseriesexplorer.readthedocs.io/en/latest/>.
- 930 Land Cover Piemonte: https://www.geoportale.piemonte.it/geonetwork/srv/api/records/r_piemon:006cb751-4274-4ac3-a5bd-5bb3f1bbd251, last access: 8 June 2022.
- Regione Piemonte - flood events 2019:
<http://www.sistemapiemonte.it/eXoRisorse/dwd/servizi/EventiAlluvionali/novembre2019/OCn3-A18-615-622-del-06042020.pdf>, last access: 13 August 2021.
- 935 Roccati, A., Faccini, F., Luino, F., Turconi, L., and Guzzetti, F.: Rainfall events with shallow landslides in the Entella catchment, Liguria, northern Italy, *Nat. Hazards Earth Syst. Sci.*, 18, 2367–2386, <https://doi.org/10.5194/nhess-18-2367-2018>, 2018.
- Roccati, A., Paliaga, G., Luino, F., Faccini, F., and Turconi, L.: Rainfall Threshold for Shallow Landslides Initiation and Analysis of Long-Term Rainfall Trends in a Mediterranean Area, *Atmosphere*, 11, <https://doi.org/10.3390/atmos11121367>, 2020.
- 940 Rossi, M., Guzzetti, F., Reichenbach, P., Mondini, A. C., and Peruccacci, S.: Optimal landslide susceptibility zonation based on multiple forecasts, *Geomorphology*, 114, 129–142, <https://doi.org/10.1016/j.geomorph.2009.06.020>, 2010.
- Sassa, K., Fukuoka, H., Scarascia-Mugnozza, G., and Evans, S.: Earthquake-induced-landslides: distribution, motion and mechanisms, *Soils and Foundations*, 36, 53–64, <https://doi.org/10.1016/j.sandf.2014.06.001>, 1996.
- 945 Scheip, C. M. and Wegmann, K. W.: HazMapper: a global open-source natural hazard mapping application in Google Earth Engine, *Nat. Hazards Earth Syst. Sci.*, 21, 1495–1511, <https://doi.org/10.5194/nhess-21-1495-2021>, 2021.
- Terrell, G. R. and Scott, D. W.: Variable kernel density estimation, *The Annals of Statistics*, 1236–1265, 1992.

950 Trigila, A., Frattini, P., Casagli, N., Catani, F., Crosta, G., Esposito, C., Iadanza, C., Lagomarsino, D., Mugnozza, G. S.,
and Segoni, S.: Landslide susceptibility mapping at national scale: the Italian case study, *Landslide Science
and Practice: Volume 1: Landslide Inventory and Susceptibility and Hazard Zoning*, 287–295, 2013.

Yu, B., Chen, F., and Muhammad, S.: Analysis of satellite-derived landslide at Central Nepal from 2011 to 2016,
Environmental Earth Sciences, 77, 331, <https://doi.org/10.1007/s12665-018-7516-1>, 2018.

955